nature physics

Supplementary information

https://doi.org/10.1038/s41567-024-02529-6

Non-Abelian braiding of Fibonacci anyons with a superconducting processor

In the format provided by the authors and unedited

Supplementary Information: Non-Abelian braiding of Fibonacci anyons with a superconducting processor

CONTENTS

I. THEORY

A. Non-Abelian anyons

Anyons are quasiparticles in two dimensional space that can break the fermion-boson dichotomy [1]. Among them, non-Abelian anyons obey non-Abelian braiding statistics: they have multiple fusion channels, and their interchanges yield unitary operations in a space spanned by topologically degenerate wavefunctions, rather than merely phase factors like fermions, bosons, and Abelian anyons [2]. Fusion rules describe the possible fusion outcomes when fusing anyons, denoted as,

$$a \times b = \sum_c N_{ab}^c c, \tag{S1}$$

where a, b, and c are labels of anyons, N_{ab}^c is a nonnegative integer and the sum is over the complete set of labels. The quantum dimension of a specific anyon a is defined as the rate at which the Hilbert space enlarges as anyons are added, denoted as d_a. The quantum dimension satisfies,

$$d_a d_b = \sum_c N_{ab}^c d_c. \tag{S2}$$

Here we briefly introduce the F- and R-moves of anyons. The R-move exchanges the positions of two anyons and yields a phase factor (Fig. S1**a**). One uncommon property of non-Abelian anyons is that the phase factor has multiple values, different from the situation of bosons, fermions, and Abelian anyons. According to the spin-statistics theorem, the phase factor originates from three parts. First, the composite of a and b rotates clockwise by π, resulting in a phase factor of $e^{i\pi J_c}$. In the perspective of b, a winds around b anticlockwise by π, resulting in a phase factor of $e^{-i\pi J_a}$. Similarly, b winds around a anticlockwise by π, resulting in a phase factor of $e^{-i\pi J_b}$. Thus, the total additional phase factor of exchanging a and b that fusing to c is $R^c_{ab} = e^{i\pi(J_c - J_a - J_b)}$. This phase factor is not unique since the type of c is not unique in the non-Abelian case.

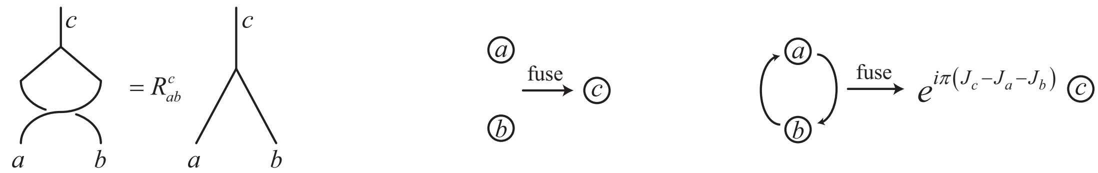

FIG. S1. Sketch of the R-move. **a**, The R-move exchanges the positions of a and b before their fusion. The resulting state is related to the original state with an addition phase factor R^c_{ab}. **b**, The case of a and b fusing into c. **c** a and b exchange their positions before fusing into c. This process produces a quasiparticle c rotating at an angle of π. According to the spin-statistics theorem, the total additional phase factor is $R^c_{ab} = e^{i\pi(J_c - J_a - J_b)}$ connected to multiple types of c.

We give a concrete description of the F-move. Mathematically, there is an axiom satisfied by the fusion rules of an anyon model [3]:

$$(a \times b) \times c = a \times (b \times c)\,, \tag{S3}$$

which is natural since the total charge of three anyons a, b, and c should be an intrinsic property of the system. Now we consider the topological Hilbert space describing the different ways to fuse a, b, and c and yield a total charge d,

$$V^d_{abc} \cong \bigoplus_e V^e_{ab} \otimes V^d_{ec} \cong \bigoplus_f V^f_{bc} \otimes V^d_{af}. \tag{S4}$$

For example, $V^e_{ab} \otimes V^d_{ec}$ represents the Hilbert space of a and b fusing into e first, and then e and c fusing into d. The corresponding orthonormal bases of V^d_{abc} can be defined in two different ways,

$$|(a \times b) \times c \to d; e\rangle \equiv |a \times b \to e\rangle \otimes |e \times c \to d\rangle\,, \tag{S5}$$

$$|a \times (b \times c) \to d; f\rangle \equiv |a \times f \to d\rangle \otimes |b \times c \to f\rangle\,. \tag{S6}$$

These two sets of bases are related by a six-index tensor F:

$$|(a \times b) \times c \to d; e\rangle = \sum_f F^{abe}_{cdf}\, |a \times (b \times c) \to d; f\rangle. \tag{S7}$$

B. Anyonic quantum computing

We have shown that changing fusion bases leads to a linear transformation F, and braiding anyons leads to a phase factor related to their total charge. Thus, we can encode the quantum information in such a topologically protected Hilbert space. For example, consider two non-Abelian anyons a and b with total charge c, the R-move produces a phase factor R^c_{ab}, which is basically the phase shift gate in the quantum circuit model. The topological protection of fusion space comes from the long-range entanglement between anyons far apart.

For a condensed matter system supporting anyonic quantum computing, the low temperature can protect the quantum information encoded in the degenerate ground states from gapped excitations [4]. In contrast, the quantum information is usually encoded in two different energy levels in the conventional quantum computer, where suppressing excitations means keeping the quantum state at the ground state $|0\rangle$. Meanwhile, the digital simulation of a spin model supporting anyonic excitations corresponds to an error correction scheme. Only a long string operator with a specific form can cause an undetectable error on the logical qubit [2].

We note that in Eq. (S7), we can use the F-move to change the first fusion from $a \times b$ to $b \times c$. We can also change the position of anyons with the R-move when knowing their total charge. Combining these two operations allows us to change the position of anyons arbitrarily, which will provide a representation of the braid group. For example, we consider the process described by the following equation:

$$\begin{aligned} |(a \times b) \times c \to d; e\rangle &= \sum_f F^{abe}_{cdf}\, |a \times (b \times c) \to d; f\rangle = \sum_f R^f_{bc} F^{abe}_{cdf}\, |a \times (c \times b) \to d; f\rangle \\ &= \sum_f F^{adf}_{bcg} R^f_{bc} F^{abe}_{cdf}\, |(a \times c) \times b \to d; g\rangle. \end{aligned} \tag{S8}$$

To swap the position of anyons b and c, we need to know the fusion result of them. Since we know that the fusion result of a and b is e, and the total charge of a, b, and c is d, the fusion result of b and c is a superposition of different f with the amplitude of F^{abe}_{cdf}. Then, we can use the R-move described by R^{f}_{bc} to swap the positions of b and c. Finally, we change the fusion basis back to first fusing a and b with another F-move. This operation is called the braiding operator B with

$$B^{abe}_{cdg} = \sum_{f} F^{adf}_{bcg} R^{f}_{bc} F^{abe}_{cdf}. \tag{S9}$$

Denoting the exchange operation of the i-th and $i+1$-th particles as σ_i, it is the generator of the braid group and has the following property:

$$\sigma_i \sigma_{i+1} \sigma_i = \sigma_{i+1} \sigma_i \sigma_{i+1}, \tag{S10}$$

which is known as the Yang-Baxter equation. In our encoding scheme, we initialize the logical qubits as particle-antiparticle pairs with trivial total charge. The logical state is an eigenstate of σ_1 with the eigenvalue being $R^{\mathbf{1}}_{a\bar{a}}$ since

$$\sigma_1 |\bar{0}\rangle^{\otimes N} = \left|(a \times \bar{a})_{\mathbf{1}}, \left(b \times \bar{b}\right)_{\mathbf{1}}, \cdots \right\rangle = R^{\mathbf{1}}_{a\bar{a}} |\bar{0}\rangle^{\otimes N}. \tag{S11}$$

Meanwhile, the eigenstate of σ_2 is $\sigma_1\sigma_2|\bar{0}\rangle^{\otimes N}$ with the same eigenvalue because

$$\sigma_2\sigma_1\sigma_2|\bar{0}\rangle^{\otimes N} = \sigma_1\sigma_2\sigma_1|\bar{0}\rangle^{\otimes N} = R^{\mathbf{1}}_{a\bar{a}}\sigma_1\sigma_2|\bar{0}\rangle^{\otimes N}, \tag{S12}$$

which is verified by our experimental results shown in Fig. 4 in the main text.

C. String-net model

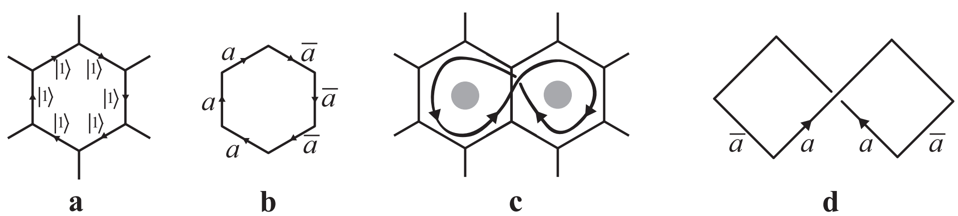

FIG. S2. String-net and the fattened lattice picture. **a**, A closed loop on the string-net. Each edge is associated with one qubit. **b**, The corresponding world line of **a**, where one particle-antiparticle pair is created and fused. **c**, A string operator in the fattened lattice picture. The strings that are not on the grid can be absorbed into the honeycomb lattice, which produces a superposition of original string-net configurations. The shaded regions in the centers of the hexagons are forbidden regions in the fattened lattice picture for the strings. **d**, The corresponding world line of **c**. Two particle-antiparticle pairs are created, one particle from the pair on the right is exchanged with the particle from the left pair in a counterclockwise sense, and then both pairs are fused. This process can also be described as braiding two anyons.

The string-net is purposed to provide a physical mechanism for "doubled" topological phases [5, 6]. In this work, we focus on the string-net model defined on the 2D honeycomb lattice, where each edge on this lattice is occupied by a spin. The degree of freedom of the spin is $N+1$, where N is the number of string types. The string-net pictures can be regarded as the world lines of anyons. We use a simple example with $N=1$ to illustrate this. A close loop shown in Fig. S2**a** is denoted by the state $|1\rangle^{\otimes 6}$. This world line represents a process in which one particle-antiparticle pair is created and fused, as shown in Fig. S2**b**. The direction of time is irrelevant since we consider the original Levin-Wen model which is isotropic [5, 6].

There is also an alternative graphical representation called fattened lattice which provides a simple visual technique for understanding the Hamiltonian and quasiparticle excitations. In this picture, strings can exist on top of the original honeycomb lattice but can not cross the forbidden area in the center of each hexagon. A simple example of the closed string operator drawn in the fattened lattice picture and the corresponding world line are shown in Fig. S2**c** and S2**d**, respectively. The fattened lattice picture can be reduced to a linear combination of the original honeycomb lattice with some local transformations denoted as F and Ω, which will be introduced later.

Here we describe the basic picture of string-net condensation Ref. [5]. The topological phase occurs when the string-net is highly fluctuating and condensed. The condition of a dominating kinetic energy constraints that only string-net configurations with certain modes exist. These local constraints describe the linear relationship between amplitudes Φ of string configurations that differ by local transformations. They can be put in the following graphical form:

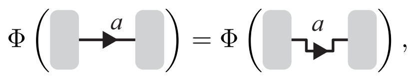

(S13a)

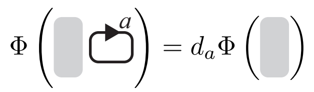

(S13b)

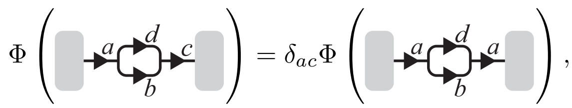

(S13c)

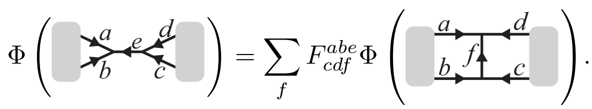

(S13d)

The shaded regions represent the rest parts of the configurations, which are the same on both sides of the equations. Meanwhile, if the strings meeting at a bivalent or trivalent point do not satisfy the branching rules (corresponding to the fusion rules of the underlying anyon model), the value of the symbol F related to this configuration is unphysical. We set $F = 0$ in this case, which implies that the ground state configurations are required to meet the branching rules. In this work, we only consider the self-dual model where all strings are unoriented, namely $a^* = a$. Thus, we sometimes do not draw the arrows on the string-net configurations and do not distinguish the conjugation of F symbols (F is real-valued).

We note that the values of F and d can not be chosen arbitrarily, otherwise the local constraints of Eq. (S13) may be not self-consistent. Only F and d meeting the following conditions support the well-defined string-net condensed wavefunction (up to a trivial rescaling):

$$\text{physicality}: \quad F^{ijm}_{kln}\delta_{ijm}\delta_{klm^*} = F^{ijm}_{kln}\delta_{iln}\delta_{jkn^*} \tag{S14a}$$

$$\text{pentagon equation}: \sum_{n=1}^{N} F^{mlq}_{kpn}F^{jip^*}_{mns}F^{jsn}_{lkr} = F^{jip^*}_{q^*kr}F^{r^*iq^*}_{mls} \tag{S14b}$$

$$\text{unitarity}: \quad \left(F^{ijm}_{kln}\right)^* = F^{lin}_{jkm^*} \tag{S14c}$$

$$\text{tetrahedral symmetry}: F^{ijm}_{kln} = F^{jim}_{lkn^*} = F^{lkm^*}_{jin} = F^{imj}_{k^*nl}\frac{v_m v_n}{v_j v_l} \tag{S14d}$$

$$\text{normalization}: \quad F^{ii^*\mathbf{1}}_{j^*jk} = \frac{v_k}{v_i v_j}\delta_{ijk} \tag{S14e}$$

where $v_i = \sqrt{d_i}$. We note that the physicality [Eq. (S14a)] and unitarity [Eq. (S14c)] do not apply to the general case [7]. They are purposed to avoid the nonphysical solutions and can realize topological phases that do not break time-reversal symmetry [6, 7].

D. Fixed-point Hamiltonian

The linear relationship described in Eq. (S13) can uniquely determine the ground state wavefunction Φ, which describes the amplitude of string-net configurations. The corresponding Hamiltonian is composed of two terms:

$$H = -\sum_v Q_v - \sum_p B_p, \tag{S15}$$

where Q_v corresponds to the fusion rules of anyons on the vertices and $B_p = \sum_s a_s B_p^s$ on the plaquettes provides dynamics. The $s = 0, 1, \cdots N$ represents the different string types. Each Q_v involves three strings connected to one vertex and each B_p involves six strings of a plaquette and six strings connected to this plaquette. The Q_v constrains that all the strings meeting on the same vertex to satisfy the fusion rules, which can be represented as,

$Q_v \Big|$ 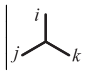 $\Big\rangle = \delta_{ijk} \Big|$ 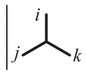 $\Big\rangle$, where $\delta_{ijk} = \begin{cases} 1, & \text{if } \{i,j,k\} \text{ is allowed,} \\ 0, & \text{otherwise.} \end{cases}$ (S16)

The B_p^s can be easily understood in the fattened lattice picture. It adds a loop of string type s cycling the shaded region, which is

$B_p^s \Big|$ 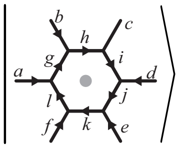 $\Big\rangle = \Big|$ 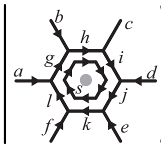 $\Big\rangle = \sum_{mnopqr} F^{alg^*}_{sm^*r} F^{bgh^*}_{sn^*m} F^{chi^*}_{so^*n} F^{dij^*}_{sp^*o} F^{ejk^*}_{sq^*p} F^{fkl^*}_{sr^*q} \Big|$ 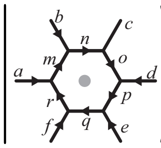 $\Big\rangle$. (S17)

The coefficients a_s is selected to be $a_s = d_s / \sum_{i=0}^{N} d_i^2$. This choice corresponds to a topological phase with a smooth continuum limit [5], and makes B_p a projector. This can be proved by:

$$(B_p)^2 = \left(\sum_s a_s B_p^s\right)^2 = \frac{1}{D^2}\sum_{sr} d_s d_r B_p^s B_p^r = \frac{1}{D^2}\sum_{srt} d_s d_r \delta_{rst} B_p^t = \frac{1}{D^2}\sum_{st} d_s^2 d_t B_p^t = \frac{1}{D}\sum_t d_t B_p^t = \sum_s a_s B_p^s = B_p, \tag{S18}$$

where $D = \sum_s d_s^2$ is the total quantum dimension of the model. This proof utilizes $B_p^s B_p^r = \sum_t \delta_{rst} B_p^t$ which is proved in Ref. [5], and $d_a d_b = \sum_c \delta_{abc} d_c$, which is Eq. (S2) in multiplicity-free case.

For the Fibonacci string-net model, the nontrivial fusion rule reads

$$\tau \times \tau = \mathbf{1} + \tau, \tag{S19}$$

where $\mathbf{1}$ denotes a null string (vacuum). We record the state of an isolate string loop as $|\mathbf{1}\rangle + x|\tau\rangle$. This state does not change when adding a null loop (implementing B^0), which is trivial. We also require that the state is unchanged (up to a rescaling factor) when adding a loop of τ. The resulting state is $|\mathbf{1}\times\tau\rangle + x|\tau\times\tau\rangle = x|\mathbf{1}\rangle + (x+1)|\tau\rangle$. One solution of x is $\frac{1+\sqrt{5}}{2}$, which is the quantum dimension of the Fibonacci anyon d_τ. The other solution is $\frac{1-\sqrt{5}}{2}$, which is associated with the Yang-Lee singularity [8] and does not correspond to a physically realizable topological phase for string-net model [5].

Another important property of B_p is that it "commutes" with the F-moves [9]. In the main text, we have shown that we can change the geometry of the string-net with F-moves. Such deformation does not change the measurement result of B_p, which always corresponds to adding a type-s string loop in the fattened lattice picture. The consistency of this interpretation is guaranteed by Mac Lane's coherence theorem as long as the deformation obeys the local rules. As an example, here we give a detailed proof for the deformation from a hexagon to a pentagon with the explicit expression given by Eq. (S17), combined with the constraints of the F-matrix of Eq. (S14). We denote the operator of adding a virtual loop of type-s to a pentagon in the fattened lattice picture as D_p^s. The expected value of B_p^s under arbitrary state $|\Psi\rangle$ can be calculated according to Eq. (S17), which is

$\langle\Psi| B_p^s |\Psi\rangle = \sum_{a\sim r} F^{alg^*}_{sg^*l} F^{bgh^*}_{sh^*g} F^{chi^*}_{si^*h} F^{dij^*}_{sj^*i} F^{ejk^*}_{sk^*j} F^{fkl^*}_{sl^*k} Tr \Bigg(\Big\langle$ 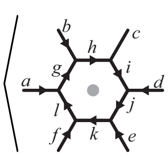 $\Big|\Psi\rangle\langle\Psi\Big|$ 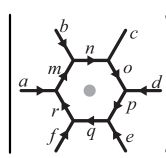 $\Big\rangle\Bigg)$, (S20)

where "Tr" means partial tracing over other strings (qubits) and $\sum_{a\sim r}$ represent the sum over all indices from "a" to "r". Meanwhile, the matrix elements of D_p^s can be calculated by:

$D_p^s \Big|$ 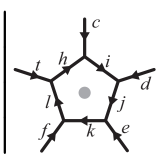 $\Big\rangle = \Big|$ 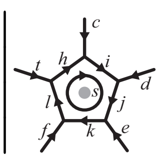 $\Big\rangle = \sum_{nopqr} F^{tlh^*}_{sn^*r} F^{chi^*}_{so^*n} F^{dij^*}_{sp^*o} F^{ejk^*}_{sq^*p} F^{fkl^*}_{sr^*q} \Big|$ 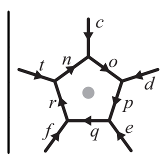 $\Big\rangle$. (S21)

Thus, the expected value of D_p^s on the deformed lattice corresponding to the state $F\,|\Psi\rangle$ can be written as

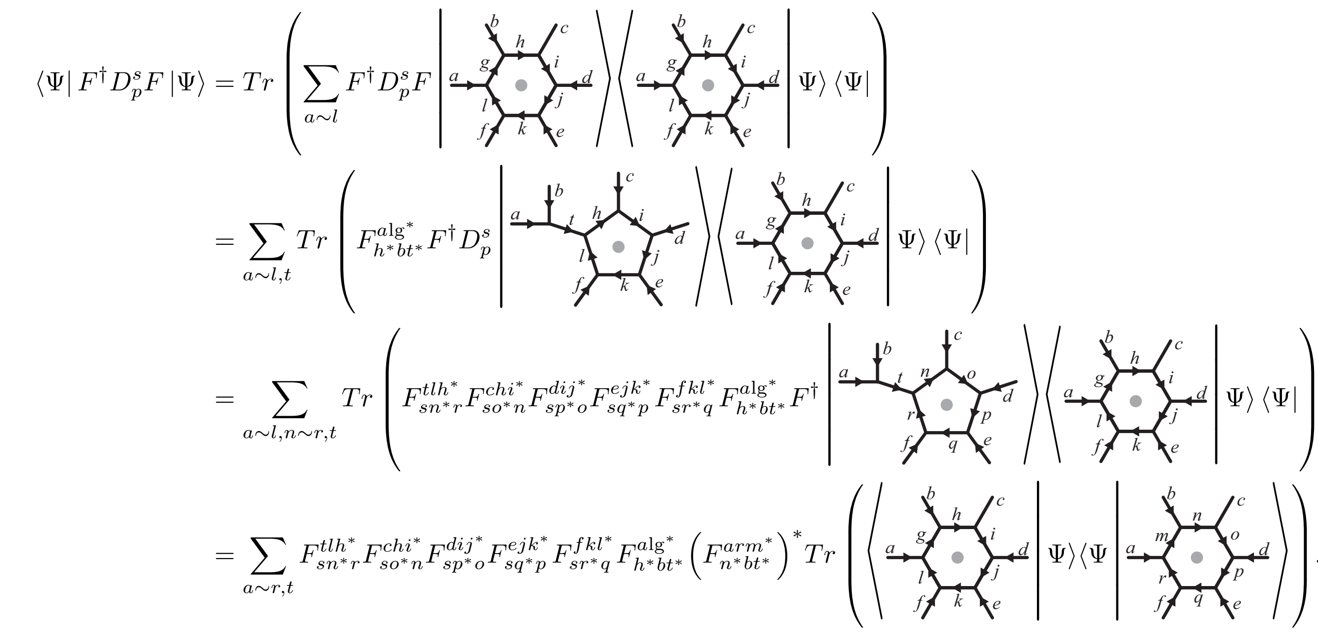

(S22)

Based on the unitarity of the F-matrix from Eq. (S14c), $\left(F^{arm^*}_{n^*bt^*}\right)^* = F^{bat^*}_{rn^*m}$. We can also derive that $F^{\mathrm{alg}^*}_{h^*bt^*} = F^{lag^*}_{bh^*t}$, $F^{tlh^*}_{sn^*r} = F^{n^*sh}_{ltr}$, and $F^{bat^*}_{rn^*m} = F^{n^*rt}_{abm}$ according to the tetrahedral symmetry [Eq. (S14d)] of the Levin-Wen model. With the pentagon equation, we obtain

$$\sum_t F^{lag^*}_{bh^*t} F^{n^*sh}_{ltr} F^{n^*rt}_{abm} = F^{n^*sh}_{gbm} F^{m^*sg}_{lar} = F^{\mathrm{alg}^*}_{sm^*r} F^{bgh^*}_{sn^*m}, \tag{S23}$$

where the second equal sign uses the tetrahedral symmetry again. Thus, the expected value of B_p on the original hexagon equals the expected value of D_p on the pentagon, which can be further reduced to the expected value of the operator that adds a virtual loop on a tadpole [9, 10].

E. Quasiparticle excitations

The quasiparticle excitations can be created in pairs and have a stringlike structure. The position of such a string operator is unobservable in the string-net condensed state, and its endpoints behave like independent particles. If the string operator forms a loop with no endpoints, it should commute with the Hamiltonian and become unobservable. The string loops can be directly drawn in the fattened lattice picture. Meanwhile, we need a new correspondence relationship to map the cross in fattened lattice to a linear combination of string-net configurations [5]:

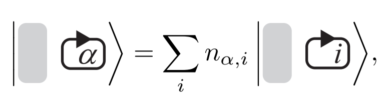

(S24a)

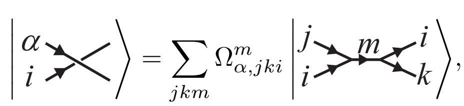

(S24b)

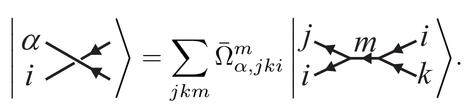

(S24c)

In this work, we only focus on the "simple" string operators where $j = k = \alpha$. More specifically, we only handle a subcategory $\{1,\tau\}$ of the Fibonacci string-net model and ignore its counterpart with the opposite chirality. The Fibonacci anyon is characterized by type-1 simple string operators.

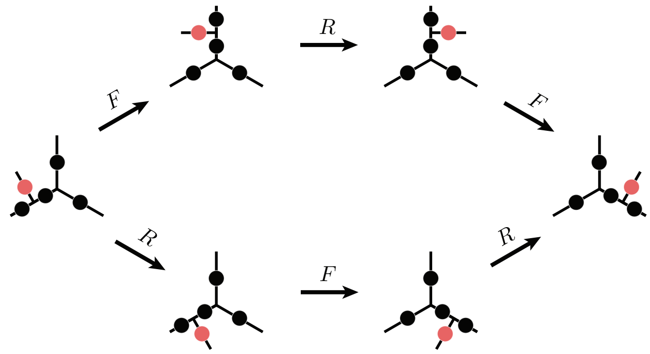

FIG. S3. Two equivalent paths to move one tail to the destination, which describes the hexagon equation for anyon models.

We have shown that the F-move commutes with the B_p operator in Eq. (S22) based on the pentagon equation Eq. (S14b). Thus, the string operator can freely move in the plaquette while remaining unobservable. A similar statement applies to crossing different plaquettes with the R-move, which is based on the hexagon equation. This relationship can be represented by the equivalence of the two processes shown in Fig. S3, abbreviated as $RFR = FRF$. The corresponding graphical representation with the Ω notation is:

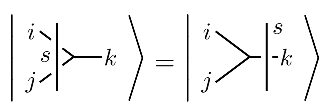

(S25)

There is some ambiguity when defining the endpoints of the string operator. However, this ambiguity does not influence the mutual statistics of the quasiparticle excitations since it only depends on the topology of how string operators braid instead of the local effect at the endpoints [6]. In this work, we define the endpoints as the tails on the string-net configuration [11], which is directly reduced from an open string in the fattened lattice picture. The reduction can be performed by the linear relationship in Eq. (S13) and (S24). Under the tailed string-net picture, the algebraic form of the closed simple string operator is the same as that in the Ref [5]. Since the quasiparticle excitations are clearly located at the tails, we can conveniently express the mutual statistics with this figure.

Here we give an example of the shortest "simple" type-s string operator B_p^s, which is also denoted as $W_s(\partial p)$. Since the closed string operator B_p does not cross the honeycomb lattice, we can reduce a fattened lattice picture to a linear combination of string-net configurations with only F-moves. As discussed in Sec. I A, the F-moves change the fusion sequences of anyons. The algebraic form of F-move is given by a six-index tensor F that explains how the outcomes change under the control of these four anyons. We illustrate this process in Fig. S4**a**, where the "controlling" strings are marked in green and the fusion outcomes are marked in red.

In Fig. S4**b** and **c**, we plot the same process described by B_p^s in the fattened lattice picture and the tailed string-net picture, respectively. In Fig. S4**b**, we show how to change a fattened lattice picture to a superposition of string-net configurations, where the corresponding coefficients and the Dirac kets are omitted for brevity. We note that the superposition coefficients in Fig. S4**b** are equal to that given in Eq. (S17) despite the different forms. We can also recognize this Wilson loop as the process of creating two quasiparticles (tails in Fig. S4**c** and **d**) and fusing them later. The blue strings in these two figures represent the "occupied" (type-1) string [5] to show some of the valid string-net configurations in this process for the Fibonacci string-net model.

The reduction of closed string operator crossing different plaquettes in fattened lattice picture to the superposition of string-net configurations requires the relationship characterized by the Ω-matrix, as shown in Eq. (S24), in addition to those given by the F-matrix. We still use the tailed string-net picture which better illustrates this process and is more convenient in the design of quantum circuits. An example of describing the same process is shown in Fig. S5. We note that the Ω-matrix and the R-matrix characterize the same relationship between different configurations since they are both solved from the hexagon equation.

In this work, we use the tailed string-net configuration to better illustrate the position of the electric charge τ in the absence of the fluxon (for further information about the full dyon spectrum, see Ref. [11]). The electric charge can be defined with an extra Q_v operator on the tail, which is:

$$Q_v \left| \vdash s \right\rangle = \delta_{s,0} \left| \vdash s \right\rangle . \tag{S26}$$

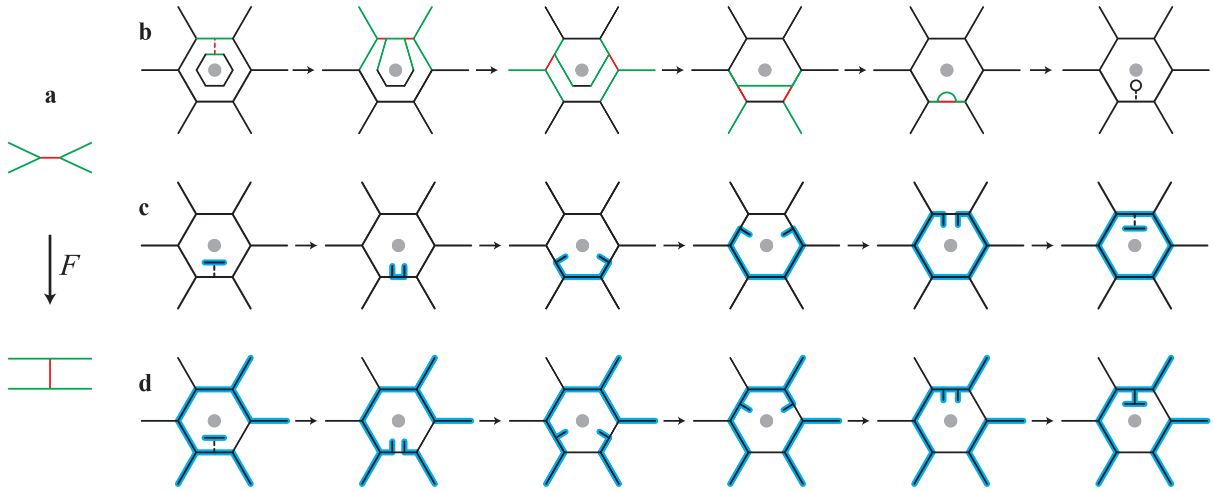

FIG. S4. Description of the shortest closed simple string operator $W(\partial p)$ in different pictures. **a**, The F-move on unoriented strings. The green strings are "controlling" string which is unchanged after the F-move. The red strings represent fusion outcomes that change according to the known string types to be fused. **b**, The transformation from the fattened lattice to the superposition of string-net configurations after implementing the $W(\partial p)$ operator on the string-net wavefunction. The coefficients describing the linear transformation are omitted. **c** and **d**, The tailed string-net picture describing the same process as in **b**. We omit the string connecting the endpoints of the two tails. This picture shows the process of creating two quasiparticles (blue strings) and annihilating them to vacuum more intuitively. We use the thick blue lines to represent the type-1 strings in the Fibonacci string-net model whose fusion rule is given by Eq. (S19). For clarity, here we present two examples of the valid string-net configurations in **c** and **d**, respectively. The dotted lines represent the strings that are known to be vacuum.

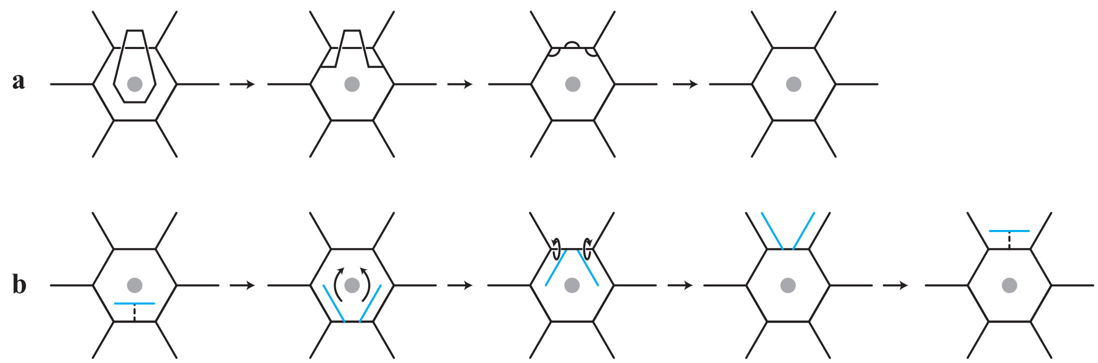

FIG. S5. A closed string operator crossing the honeycomb lattice twice. **a**, Reduction from the fattened lattice picture to a superposition of string-net configurations. **b**, The tailed string-net picture describing the same process as **a**. The rotations shown in the third subgraph contain a clockwise R move and an anticlockwise R^{-1} move.

The creation, movement, and fusion of these electric charges have been introduced as the endpoints of the string operators (tails) in the main text. With the F- and R-move, these quasiparticles can be moved to demonstrate their topological spin and mutual statistics. The non-Abelian mutual statistics of Fibonacci anyon provide a promising way to define logical qubits and operations in topological quantum computation, which is demonstrated in our experiment.

F. Closed string operators in the tailed string-net picture

We have introduced and experimentally demonstrated that we can detect the electric charge with the extra Q_v operator defined in Eq. (S26). We also would like to further introduce an intuitive way to derive the nonlocal closed string operator to detect the quasiparticle excitations, which is known as Ocneanu's tube algebra in TQFT [7]. The definition of these different closed string operators characterizing the same topological charge is important for the error correction scheme in fault-tolerant quantum computing.

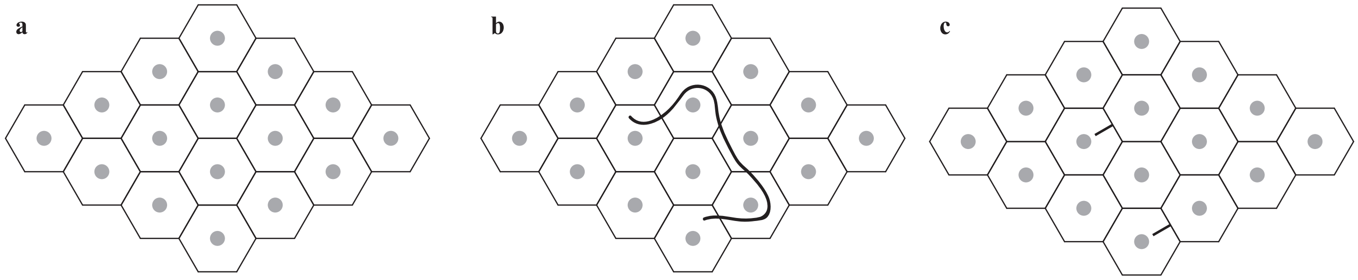

FIG. S6. The string operator in fattened lattice and the tailed string-net picture. **a**, The ground state of the original string-net picture. **b**, An open string operator in the fattened lattice picture. **c**, The reduced tailed string-net picture corresponding to the string operator of **b**.

In the tailed string-net picture shown in Fig. S6**a**, the action of an open string operator that creates quasiparticle excitations can be directly drawn on it as shown in Fig. S6**b**. This string state can be decomposed to a linear combination of tailed string-net with the geometry shown in Fig. S6**c**. To derive the algebraic form of the fixed-point Hamiltonian, we first consider a closed string operator containing one tail as shown in Fig. S7**a**. We note that this closed string operator is defined on strings far from the tails, whose algebraic form does not change after adding the tails. Since there is no tail in other plaquettes (or all other tails are vacuum strings), this close string operator can be continuously transformed to a smaller one as shown in Fig. S7**b**. According to the hexagon equation of Eq. (S25), the closed string operator can be reduced to the form shown in Fig. S7**c**.

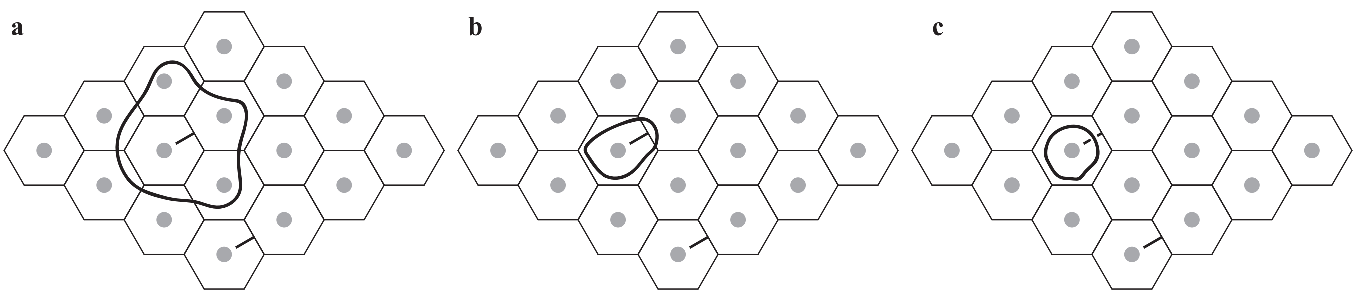

FIG. S7. Topological equivalent closed string operators. **a**, A large close string operator containing one tail. Its algebraic form is the same as the one in the original string-net picture. **b**, A smaller topological equivalent closed string operators. **c**, The smallest topological equivalent closed string operators.

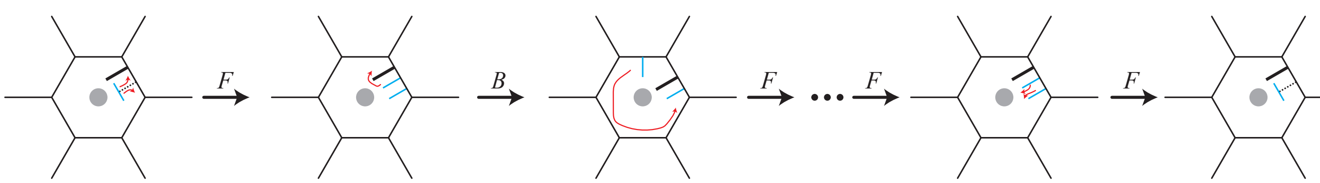

FIG. S8. A description of simple closed string operator O^x_p in the tailed string-net picture. We can directly derive the algebraic form in Eq. (S27) according to this figure.

To derive the algebraic form of this closed string operator, we rewrite it as a process shown in Fig. S8. The process can be described as: (1) create one pair of type-x excitations near the tail; (2) move one of the quasiparticles across the tail with a B operator given in Eq. (S9); (3) wind the above quasiparticle around this plaquette; (4) annihilate the two quasiparticles to vacuum. The corresponding algebraic form of this closed string operator O^x_p can be written as:

$O^x_p \Big|$ 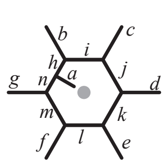 $\Big\rangle = \Big|$ 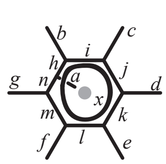 $\Big\rangle = \sum_{xopqrstu} B^{ahn}_{uxo} F^{bih}_{xop} F^{cji}_{xpq} F^{dkj}_{xqr} F^{elk}_{xrs} F^{fml}_{xst} F^{gnm}_{xtu} \Big|$ 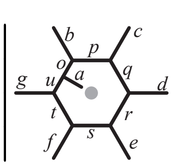 $\Big\rangle$. (S27)

This closed string operator can characterize the topological charge of an area. This corresponds to a basic fact that the way to detect a particle is to interact with it. In this double-Fibonacci model, we can detect whether there is a τ charge by surrounding this area with a τ anyon.

Similar to the extra Q_v defined in Eq. (S26), we can define the extra B_p operator O_p as:

$$O_p = \frac{1}{D}\sum_s d_s O_p^s. \tag{S28}$$

It can be easily proved that the O_p is a projector from the fattened lattice picture shown in Fig. S7. The ground state is the eigenstate of O_p with the eigenvalue of 1, since the ground state does not have tails and the operator O_p is reduced to B_p. Meanwhile, the measurement result of O_p on the result state $|\psi_{\tau\tau}\rangle$ after implementing a type-τ string operator is zero. Now we explain this statement with a basic physical intuition: the state with a pair of quasiparticle excitations should be orthogonal to the state with their time reversal counterpart excitations. Considering the ground state on a closed loop with one string, the overlap between states with two kinds of quasiparticle excitations related by the time-reversal symmetry is zero for the self-dual model:

$$\begin{aligned} 0 = \frac{1}{D^2}\sum_{ij} d_i d_j \left\langle {}^{\bar{s}}_{j}\!\times \middle| {}^{s}_{i}\!\times \right\rangle &= \frac{1}{D^2}\sum_{ijmn} d_i d_j F^{ii^*0}_{s^*sm} F^{jj^*0}_{\bar{s}^*\bar{s}n} R^m_{is}\left(R^n_{j\bar{s}}\right)^* \left\langle {}^{\bar{s}}_{j} \, n \, {}^{j}_{\bar{s}} \middle| {}^{s}_{i} \, m \, {}^{i}_{s} \right\rangle \\ &= \sum_{im} \frac{d_i d_m}{d_s} R^m_{is} (R^m_{i\bar{s}})^*. \end{aligned} \tag{S29}$$

For the self-dual model with time reversal symmetry, $R^m_{i\bar{s}} = (R^m_{i^*s})^{-1} = (R^m_{is})^{-1} = (R^m_{is})^*$, and

$$\left| {}^{s}_{i}\!\times \right\rangle = \sum_m F^{ii0}_{ssm} R^m_{is} \left| {}^{s}_{i} \, m \, {}^{i}_{s} \right\rangle = \sum_m F^{ii0}_{ssm} (R^m_{i\bar{s}})^{-1} \left| {}^{s}_{i} \, m \, {}^{i}_{s} \right\rangle = \left| {}^{\bar{s}}_{i}\!\times \right\rangle. \tag{S30}$$

Thus,

$$\left\langle {}^{s}_{i}\!\times \middle| {}^{s}_{i}\!\times \right\rangle = 0. \tag{S31}$$

We can directly derive that there is no "overlap" between the operator $O_p W_\tau$ and $W_\tau O_p$ for the fattened lattice representations of O_p and W_τ. Thus, the measurement result is

$$\langle \psi_{\tau\tau}| O_p |\psi_{\tau\tau}\rangle = \langle \psi| (W_\tau)^\dagger O_p W_\tau |\psi\rangle = \langle \psi| (W_\tau O_p)^\dagger O_p W_\tau |\psi\rangle = 0. \tag{S32}$$

We can conclude that the string operator W_τ defined in the tailed string-net picture can create the type-τ excitations where the corresponding $\langle O_p\rangle = 0$. The relationship shown in Eq. (S29) is associated with the braiding nondegeneracy, which is described formally in p67-p87 of Ref. [12].

G. Topological entanglement entropy

In the string-net picture, strings are connected by the trivalent (and bivalent) points (Fig. S9**a**). To make the boundary more symmetric, we attach two spins (qubits) on each string instead of one, as shown in Fig. S9**b**. These two qubits represent the same type of directly connecting strings. The entanglement entropy in the region R of the string net model can be calculated as [13]

$$S_R = -j\ln(D) - n\sum_i^N \frac{d_k^2}{D}\ln\left(\frac{d_k}{D}\right), \tag{S33}$$

where n is the number of strings along ∂R, j is the number of disconnected boundary curves in ∂R [13], and S_R is the von Neumann entropy of the reduced density matrix ρ_R. For example, region A shown in Fig. S9**b** has $n = 3$ strings along ∂A and is a simply connected region with $j = 1$. In contrast, region D shown in Fig. S9**c** has two disconnected boundary curves and twelve strings along the boundary ∂D. According to Eq. (S33), one way to calculate the topological entanglement entropy is [14]

$$S_{topo} \equiv S_A + S_B + S_C - S_{AB} - S_{BC} - S_{AC} + S_{ABC}. \tag{S34}$$

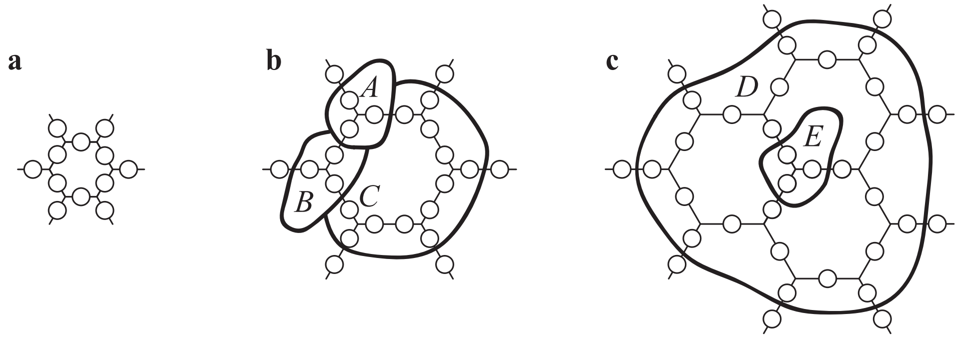

FIG. S9. Different regions on the lattice. **a**, One plaquette with twelve strings (qubits). **b**, The same lattice as **a** where each string is attached with two qubits. **c**, Three plaquettes where we define a region D with two disconnected boundary curves.

In the string-net model, the operation of copying strings on the boundary is to diagonalize the reduced density matrix and extract the information of the quantum dimensions. In fact, the derivation of Eq. (S33) is a diagonalization process of the reduced density matrix. We can deform the geometry of the string-net configurations in the region R with F-moves as shown in Fig. S10. This process corresponds to a unitary operation that can be explicitly given, though complicated. Luckily, we do not need to perform such a complicated quantum circuit if we copy the strings on the boundary. This copy operation localizes the unitary inside the region R, which does not change the entanglement spectrum of the reduced density matrix before and after the deformation.

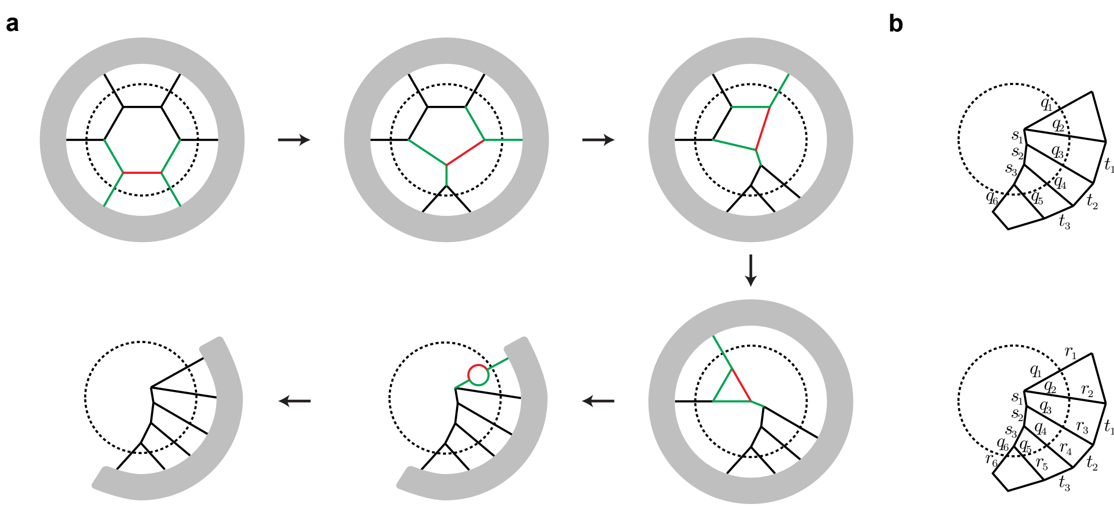

FIG. S10. Diagonalization of the reduced density matrix. After copying the strings on the boundary, the process of deforming the string-net configurations in the region R to the final geometry is a unitary process to diagonalize the reduced density matrix ρ_R. After the deformation, the reduced density matrix is a diagonal matrix whose elements are determined by the types of strings on the boundary. The measurement of S_{topo} does not actually perform the unitary consisting of the F-moves, since the entanglement spectrum does not change under a unitary operation.

In the penultimate step, we notice the linear relationship:

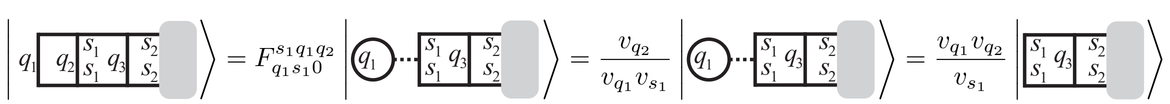

(S35)

Thus we can explicitly give the wavefunction as (without normalization),

$$\sum_{\{q,s,t\}} a_{\{q\}} \delta_{\{s\},\{t\}} \left|q_1, q_2, \cdots\right\rangle \left|s_1, s_2, \cdots\right\rangle \left|t_1, t_2, \cdots\right\rangle, \tag{S36}$$

where the coefficients can be strictly calculated as $a_{\{q\}} = \prod_{\{q\}} v_q$. In the simply connected case with $j = 1$, one can verify

$-\sum_{\{q,s,t\}} \frac{a_{\{q\}}^2}{Z} \ln\left(\frac{a_{\{q\}}^2}{Z}\right) = -\ln(D) - n\sum_i^N \frac{d_k^2}{D}\ln\left(\frac{d_k}{D}\right)$, where $Z = \sum_{\{q,s\}} a_{\{q\}}^2$ is the normalization factor. This result indicates that we can implement the quantum circuits to deform the geometry of the string-net configurations, and measure the probabilities of $|q_1, q_2, \cdots\rangle$ to obtain the information of quantum dimensions. However, the implementation of the transforming quantum circuits is complicated. An alternative way is to copy the strings on the boundaries of the region R, the state after the deformation becomes,

$$\sum_{\{q,r,s,t\}} a_{\{q\}} \delta_{\{q\},\{r\}} \delta_{\{s\},\{t\}} |q_1, q_2, \cdots\rangle |r_1, r_2, \cdots\rangle |s_1, s_2, \cdots\rangle |t_1, t_2, \cdots\rangle, \tag{S37}$$

where the copy operation introduces a Delta function $\delta_{\{q\},\{r\}}$ which is crucial in the derivation of Eq. (S33). The reduced density matrix of the region R can be calculated as (without normalization),

$$\begin{aligned}
&\underset{\{r,t,r',t'\}}{Tr}\left(\sum_{\{q,r,s,t\}} a_{\{q\}}\delta_{\{q\},\{r\}}\delta_{\{s\},\{t\}} |q\rangle |r\rangle |s\rangle |t\rangle \sum_{\{q',r',s',t'\}} a_{\{q'\}}\delta_{\{q'\},\{r'\}}\delta_{\{s'\},\{t'\}} \langle q'| \langle r'| \langle s'| \langle t'|\right) \\
&= \sum_{\{q,r,s,t\}} \sum_{\{q',r',s',t'\}} \sum_{\{r'',t''\}} a_{\{q'\}}\delta_{\{q'\},\{r'\}}\delta_{\{s'\},\{t'\}} |q\rangle |r\rangle |s\rangle |t\rangle \langle q'| \langle r'| \langle s'| \langle t'| \left(|r''\rangle \langle r''| \otimes |t''\rangle \langle t''|\right) \\
&= \sum_{\{q,r,s,t\}} \sum_{\{q',r',s',t'\}} \sum_{\{r'',t''\}} a_{\{q\}}\delta_{\{q\},\{r\}}\delta_{\{s\},\{t\}} a_{\{q'\}}\delta_{\{q'\},\{r'\}}\delta_{\{s'\},\{t'\}} |q\rangle \langle r''\ |r\rangle |s\rangle \langle t''\ |t\rangle \langle q'| \langle r'|\ r''\rangle \langle s'| \langle t'|\ t''\rangle \\
&= \sum_{\{q,r,s,t\}} \sum_{\{q',r',s',t'\}} \sum_{\{r'',t''\}} a_{\{q\}} a_{\{q'\}} \left(\delta_{\{q\},\{r\}}\delta_{\{r\},\{r''\}}\delta_{\{r'\},\{r''\}}\delta_{\{q'\},\{r'\}}\right) \left(\delta_{\{s\},\{t\}}\delta_{\{t\},\{t''\}}\delta_{\{t'\},\{t''\}}\delta_{\{s'\},\{t'\}}\right) |q\rangle |s\rangle \langle q'| \langle s'| \\
&= \sum_{\{q,s\}} a_{\{q\}} a_{\{q\}} |q\rangle |s\rangle \langle q| \langle s|.
\end{aligned} \tag{S38}$$

This is a diagonal matrix in the bases of $|q\rangle |r\rangle$, where, for example, $|q\rangle$ is the abbreviation of $|q_1, q_2, \cdots\rangle$. The transformation of string-net configurations can be individually achieved inside and outside the region R, which also does not change the entanglement spectrum. The entanglement entropy of original reduced density matrix where the strings on the boundaries are copied is also $S_R = -j\ln(D) - n\sum_i^N \frac{d_k^2}{D}\ln\left(\frac{d_k}{D}\right)$. In short, the duplication of strings on the boundary is based on that the reduced density matrix of state $\sum_i c_i |\phi_i\rangle |\phi_i\rangle |\psi_i\rangle$ is diagonal under the bases of $|\phi_i\rangle$, which is the case of Eq. (S38).

We would like to intuitively describe the difference between the string-net picture and the toric code [15] when measuring the S_{topo}. In the toric code, two adjacent qubits are connected by a string, which can be taken as a bivalent point. Thus, two regions can be defined as each containing one of the two qubits. However, the strings (qubits) in the string-net are connected by the trivalent vertices. If we do not copy the qubits on the boundaries, the qubit representing the string crossing the boundary can only be assigned to one region, which makes Eq.(S38) invalid.

II. CIRCUIT DESIGN

A. Formalism of the Fibonacci string-net model

In this work, we created the ground state of the Fibonacci string-net model and simulated the braiding of associated quasiparticle excitations, whose nontrivial fusion rule is given in Eq. (S19). Referring to Eq. (S16), the Q_v operator of the Fibonacci string-net model can be explicitly given as,

$$Q_v \left| {}_j\!\overset{i}{\perp}\!{}_k \right\rangle = \delta_{ijk} \left| {}_j\!\overset{i}{\perp}\!{}_k \right\rangle, \text{ where } \delta_{ijk} = \begin{cases} 1, & \text{if } ijk = 000, 011, 101, 110, 111, \\ 0, & \text{otherwise.} \end{cases} \tag{S39}$$

We note that $\delta_{000} = 1$ is a trivial valid fusion rule. Another trivial fusion rule is that the null string can be arbitrarily added and removed. Thus, the bivalent vertex of an anyon and its dual are always valid. This corresponds to that δ_{011}, δ_{101}, and δ_{110} are valid for Fibonacci anyons, which is self-dual $1^* = 1$. Two Fibonacci anyons may also fuse to another Fibonacci anyon, corresponding to the valid $\delta_{111} = 1$.

The B_p operator is given by the 6-index F tensor, which can be solved from Eq. (S14). Most elements can be easily calculated with the constraints of physicality and normalization. For example, $F^{\mathbf{111}}_{\tau\tau\tau} = 1$ and $F^{\mathbf{111}}_{\tau\tau\mathbf{1}} = 0$ because of the normalization of Eq.

(S14e). There are only four elements of the F-matrix that do not equal 0 or 1, which are $F^{\tau\tau\mathbf{1}}_{\tau\tau\mathbf{1}} = \frac{1}{\phi}$, $F^{\tau\tau\mathbf{1}}_{\tau\tau\tau} = \frac{1}{\sqrt{\phi}}$, $F^{\tau\tau\tau}_{\tau\tau\mathbf{1}} = \frac{1}{\sqrt{\phi}}$, and $F^{\tau\tau\tau}_{\tau\tau\tau} = -\frac{1}{\phi}$. We denote these nontrivial elements as a unitary matrix $U_F = \begin{pmatrix} 1/\phi & 1/\sqrt{\phi} \\ 1/\sqrt{\phi} & -1/\phi \end{pmatrix}$. Here ϕ is the quantum dimension of Fibonacci anyons, which is $d_\tau = \frac{1+\sqrt{5}}{2}$ solved from Eq. (S2) and Eq. (S19). Similarly, $R^{\mathbf{1}}_{\tau\tau} = e^{-4\pi i/5}$, and $R^{\tau}_{\tau\tau} = e^{3\pi i/5}$, which are solved from the hexagon equation shown in Eq. (S25) and Fig. S3 and can be denoted collectively as $U_R = \begin{pmatrix} e^{-4\pi i/5} & 0 \\ 0 & e^{3\pi i/5} \end{pmatrix}$. The conjugate of the R-matrix is also a valid solution, which describes the time reversal counterpart $\bar{\tau}$ of the Fibonacci anyon τ.

B. Circuits for the F- and R-moves of Fibonacci anyon

As shown in Eq. (S13d) and Fig. S4**a**, the F-move acts on five strings and only changes the type of one string. In the quantum circuit scheme, it is a unitary gate that acts on one qubit controlled by four qubits. The corresponding quantum circuit is shown in Fig. S11**a**. We do not need to perform this full circuit when we have some prior information about the string types for the F-move. For example, if the F-move is described by F^{aae}_{cdf}, the first two strings can be represented by one qubit and the corresponding circuit is implemented on four qubits as shown in Fig. S11**b**. The quantum circuits for other common situations are denoted as F_{3-9} and shown in Fig. S11**c**-**i**. The quantum circuit corresponding to the R move is much simpler as shown in Fig. S11**l**. When one string is known to be τ, the corresponding quantum circuit is reduced to a two-qubit controlled-U_R gate as shown in Fig. S11**m**. In our work, the physical qubits are located on the vertices of a square lattice, where two-qubit gates can be performed on two nearest neighboring qubits. We tilt the honeycomb string-net lattice 30 degrees to fit the geometry of the physical qubits, as shown in Fig. 1**b** of the main text. In Fig. 2**b** of the main text, we show the quantum circuits of the two F-moves which are used in preparing the ground state. The circuits are further compiled with a variational method provided by CPFlow [16] to fit the layout topology of the device. Similarly, the quantum circuits of other F-moves shown in Fig. S11 can also be decomposed into the form suitable for our chips, which enables us to experimentally measure the quantum dimension of the Fibonacci anyon from its mutual statistics.

C. "Copy" and "discard" qubits

In the digital quantum simulation of the string-net model, we will frequently copy and delete strings. Taking the creation process shown in Extended Data Fig 3**a** in the main text as an example, we need one qubit to "copy" the type of the bottom string at first. We also need to implement the copy operation as the first step to measure the topological entanglement entropy. To simulate the second local rule in Eq. 5(b) in the main text which deletes closed string loops, the discard operation is required. These operations can be regarded as entangling and disentangling ancillary qubits. For example, copying one string to another is performed by adding an ancillary qubit of state $|0\rangle$, implementing an X gate on this ancillary qubit controlled by the qubit that carries the information of the string to be copied. Similarly, we can discard the qubits that carry redundant information. Taking the state $\frac{a|00\rangle+b|11\rangle}{\sqrt{aa^*+bb^*}}$ as an example, where a and b are arbitrary complex numbers (not zero at the same time), we can disentangle the second qubit by implementing an X gate on it controlled by the first qubit. The processes of copying and discarding qubits are shown in Fig. S12.

D. Measuring the Q_v and B_p operators

In the main text, we have shown that we can first prepare the ground state of isolate loops and then connect them to the desired geometry with F-moves. After preparing the ground state Φ, we need to verify it by measuring all the terms in the Hamiltonian. Ref. [10] proposes detailed circuits to projectively measure the Q_v and the deformed B_p operators with ancillary qubits. Executing these circuits will introduce extra errors in the measurement stage due to limited gate fidelity and coherence time. We use an alternative method of decomposing the Q_v and B_p operators in the Pauli bases, which avoids the error of two-qubit gates in the measurement stage. The Q_v operators correspond to the fusion rule of Fibonacci anyons, where the phase of the quantum state does not contribute. Thus, we only need to measure three (or two for bivalent point) qubits in the Pauli-Z basis for each Q_v. The B_p operator is a projector on twelve qubits, and is decomposed to a sum of 99328 Pauli strings of length 12, which can be measured under 290 Pauli bases.

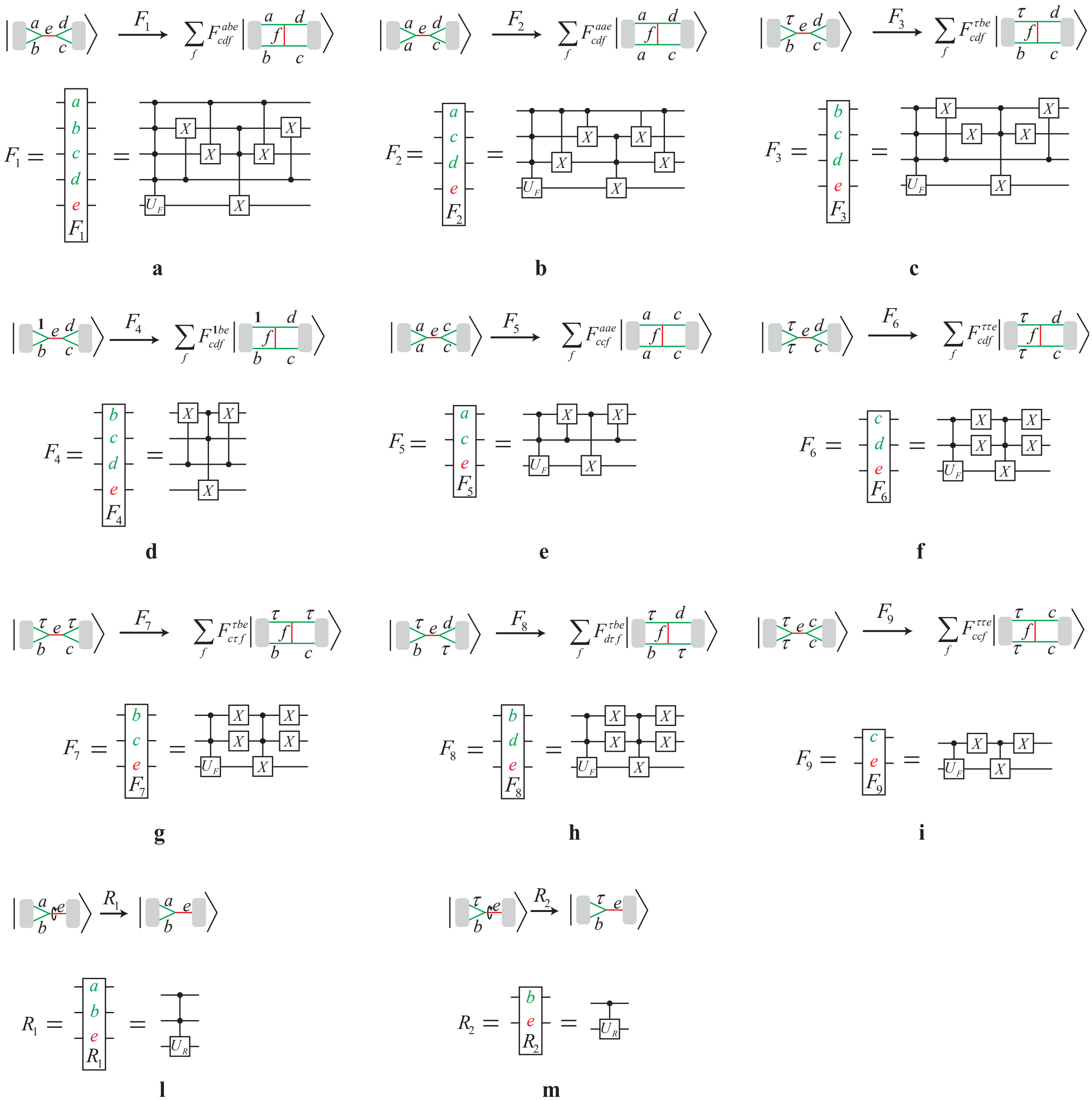

FIG. S11. The quantum circuits corresponding to the F- and R-moves under different conditions. The green strings (qubits) are unchanged after the different types of F-moves, and the red strings (qubits) corresponding to e are changed to a new string type f. The R-moves are realized by implementing a unitary gate on the red qubits controlled by the green qubits. **a**, The circuit to implement the full F-move. **b-i**, The circuit to implement the full F-move when $a = b$ (**b**), $a = \tau$ (**c**), $a = \mathbf{1}$ (**d**), $a = b$ and $c = d$ (**e**), $a = b = \tau$ (**f**), $a = d = \tau$ (**g**), $a = c = \tau$ (**h**), and $a = b = \tau$ and $c = d$ (i). **l** and **m**, The circuit to implement the R-move when $a = d = \tau$ (**l**) and $a = \tau$ (**m**).

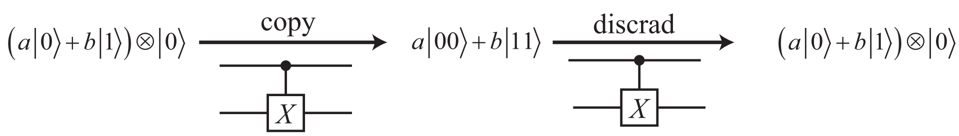

FIG. S12. The process of copying and discarding qubits. The normalization factor $\frac{1}{\sqrt{aa^*+bb^*}}$ is omitted for brevity. Initially, the information of string types is stored in the first qubit (the top line). Then a controlled-X (CX) gate copies this information to the second qubit (the bottom line). On the other hand, a CX gate implemented on two qubits which encode the same information, that is, they are on the state $a\,|00\rangle + b\,|11\rangle$, can reset the second qubit to the state $|0\rangle$ which is disentangled from the system.

E. Circuits to detect the braiding statistics

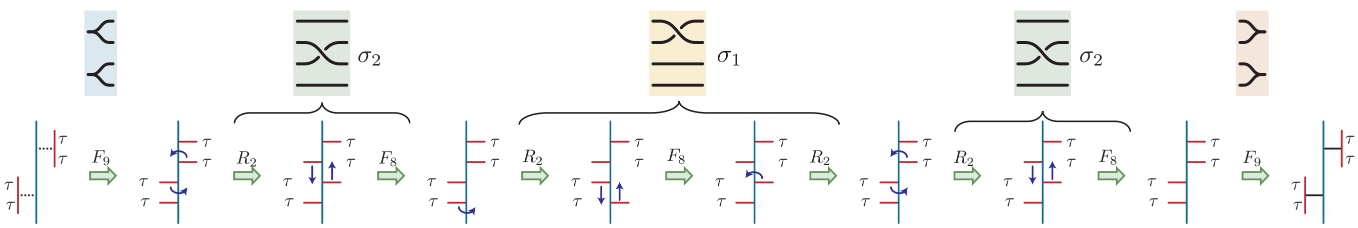

FIG. S13. Detailed process of the longest braiding sequence $\sigma_2\sigma_1\sigma_2$ shown in the main text in the string-net picture. We create two pairs of Fibonacci anyons from vacuum (the dotted lines) with the F_9 circuit. The following σ_2 is performed by implementing two R_2 circuits and one F_8 circuit, and the σ_1 is performed by implementing one R_2 circuit, one F_8 circuit, and another R_2 circuit. The circuits corresponding to specific F- and R-moves are shown in Fig. S11.

As an illustrating example, here we give a detailed description of the longest braiding sequence $\sigma_2\sigma_1\sigma_2$ shown in the main text. As shown in Fig. S13, we first create two pairs of Fibonacci anyons by adding two open type-τ strings to the string-net picture and directly connect them to the middle blue string with the F_9 circuit. Then we perform the desired braiding by moving the position of Fibonacci anyons (red strings) with F- and R-moves. In the last step, two pairs of Fibonacci anyons are detached from the middle string with another F_9 circuit, where we measure the black strings that connect them to the middle string to obtain the fusion results. After the braiding sequence $\sigma_1\sigma_2$, the corresponding logical state is an eigenstate of the braiding operator σ_2, which is explained by the Yang-Baxter equation as shown in Eq. (S12). This property is verified by our experimental results shown in Fig. 4 of the main text where implementing one more σ_2 does not change the fusion results.

The braiding sequences shown in Fig. 4 (ii), (iv), and (v) of the main text can be considered as to first prepare the logical state $\sigma_2\,|\bar{0}\rangle$ and then measure it along logical Z, $\sigma_1^\dagger\sigma_2^\dagger Z\sigma_2\sigma_1$, and $\sigma_2^\dagger Z\sigma_2$ axes, respectively. With these data, we can actually extract the whole density matrix of the experimentally prepared logical state as $\begin{pmatrix} 0.366 & -0.081-0.416i \\ -0.081+0.416i & 0.634 \end{pmatrix}$. We can also obtain a fidelity of 0.941 between this experimentally prepared logical state and the ideal state whose density matrix is $\sigma_2\,|\bar{0}\rangle\,\langle\bar{0}|\,\sigma_2^\dagger \approx \begin{pmatrix} 0.382 & -0.150-0.462i \\ -0.150+0.462i & 0.618 \end{pmatrix}$. This clearly shows that our experimental results agree well with the theoretical predictions.

III. EXPERIMENT

A. Device information

Our experiments are performed on a quantum processor with frequency-tunable transmon qubits encapsulated in a 11×11 square lattice and tunable couplers between adjacent qubits, with the overall design similar to that in Ref. [17]. The maximum resonance frequencies of the qubit and coupler are around 4.5 GHz and 9.0 GHz, respectively. The effective coupling strength between two neighboring qubits can be dynamically tuned up to -25 MHz. As shown in the Extended Data Fig. 1 of the main text, we use 27 qubits to construct the honeycomb lattice used in this experiment, with their properties shown in Fig. S14. The idle frequencies of the 27 qubits where single-qubit gates are applied are shown in Fig. S14a.The relaxation times and the Hahn echo dephasing times measured at the idle frequency of each qubit are also shown in Fig. S14b,c, with median values of $T_1 = 117\mu s$ and $T_2 = 20\mu s$, respectively. Due to the low-frequency flux noises, the Hahn echo dephasing times are much shorter than the energy relaxation times. We note that the dephasing times can be further lifted by applying more equally-spaced π pulses during the idling time. Each qubit can be measured in the computational basis using the dispersive measurement scheme, and the readout fidelities of all the qubits are summarized in Fig. S14e,f, which are used to mitigate readout errors (see Sec. III D).

B. Experimental circuit

The experimental circuit for preparing the ground state is shown in Fig. S15 and Fig. S16 (see Data availability for the explicit circuits of other experiments in this work), which contains layers of single- and two-qubit gates with different patterns (Fig. S17b). We realize arbitrary single-qubit gates by combining XY rotations and Z rotations. Single-qubit XY rotations are implemented by applying 20-ns long microwave pulses with DRAG pulse shaping [18] at qubits' respective idle frequencies, and single-qubit Z rotations are realized by the virtual-Z gate scheme [19]. We realize two-qubit CZ gates by bringing $|11\rangle$ and $|02\rangle$ (or $|20\rangle$) of the qubit pairs in near resonance at the respective interaction frequencies and activating the coupling for a specific time of 30 ns, with the calibration procedure detailed in Ref. [20]. Below we list two key steps for compiling and executing the experimental circuit.

1. *Circuit transpilation*

For a given target circuit as described in the main text, we use CPFlow [16] and Qiskit [21] to reduce its depth and recompile it with single- and two-qubit gates selected from the gate set $\{U(\theta,\varphi,\lambda),\ \mathrm{CZ}\}$, where $U(\theta,\varphi,\lambda)$ denotes a parameterized single-qubit gate with the following matrix form

$$U(\theta,\varphi,\lambda) = \begin{pmatrix} \cos\frac{\theta}{2} & -e^{i\lambda}\sin\frac{\theta}{2} \\ e^{i\varphi}\sin\frac{\theta}{2} & e^{i(\varphi+\lambda)}\cos\frac{\theta}{2} \end{pmatrix}, \tag{S40}$$

and CZ denotes the two-qubit CZ gate that fits the connectivity topology of our device. In practice, each single-qubit gate is further decomposed into a virtual Z rotation followed by an XY rotation. For each compiled experimental circuit, we further compact it before execution to reduce the impact of dephasing noise. We also avoid performing single- and two-qubit gates simultaneously in the same layer. As a result, the optimized circuit consists of a staggered arrangement of single- and two-qubit gate layers. During the execution of the circuit, we apply CPMG sequences to further minimize the impact of dephasing, which is realized by applying two Y gates (rotation around the y-axis by π angle) on qubits whose successive idle layers span more than six single-qubit gate layers.

2. *Gate optimization and benchmarking*

The experimental circuit requires multiple gates in the same layer to be implemented in parallel. In practice, we find that the performances of the parallel single-qubit idle/XY gates and two-qubit CZ gates depend strongly on the idle frequencies and interaction frequencies, which we refer to collectively as gate parameters. Learning the optimal gate parameters is essential for the successful execution of the experimental circuit, which is also challenging due to the existence of various experimental constraints, system drifts, and the exponentially large search space. In this work, we follow the idea of the Snake optimizer [22], i.e., representing the optimization objects by graphs and reducing the complex high-dimensional optimization problems into multiple simpler lower-dimensional problems, to optimize the gate parameters.

We first optimize the single-qubit gate parameters, i.e., the idle frequencies, of all the qubits. During the optimization procedure, we consider the coherence times and constrain the detunings between nearest and next-nearest qubits to construct the error model. We assess the single-qubit gate performance by simultaneous cross-entropy benchmarking (XEB), and the results are shown in Fig. S14j, with a median single-qubit gate Pauli error of 7e-4. In practice, we find that the optimized idle frequencies work for all the single-qubit gate layers in the experimental circuit, even though most of them only contain a specific part of parallel single-qubit gates.

The optimization of the two-qubit gate parameters is more subtle. Due to the engineered interactions and parasitic crosstalk, the optimal interaction frequencies of the CZ gates as well as the frequencies of the rest qubits in the system might be different for different two-qubit gate patterns. In this work, we optimize the gate parameters (including the idle frequencies of the rest qubits) for each different two-qubit gate layer in the experimental circuit, as shown in Fig. S17a. The resulting dynamical phases

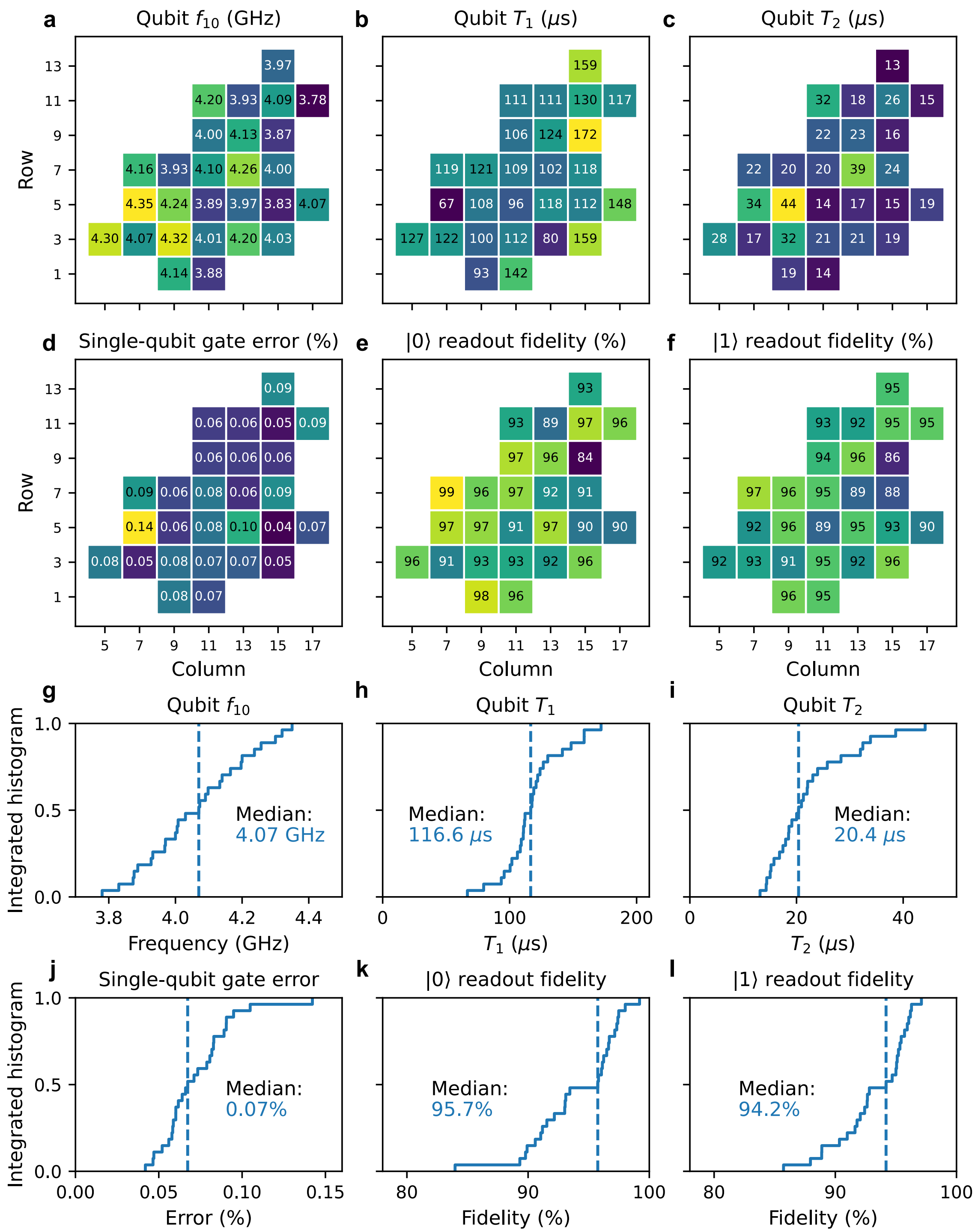

FIG. S14. Heatmaps of various single-qubit parameters and corresponding integrated histograms. a, Qubit idle frequency. **b**, Qubit relaxation time measured at the idle frequency. **c**, Qubit dephasing time measured using Hahn echo sequence. **d**, Pauli error of simultaneous single-qubit gate. **e**, Readout fidelity of the qubit $|0\rangle$ state. **f**, Readout fidelity of the qubit $|1\rangle$ state. **g-l**, Corresponding integrated histograms. Dashed lines indicate the median values.

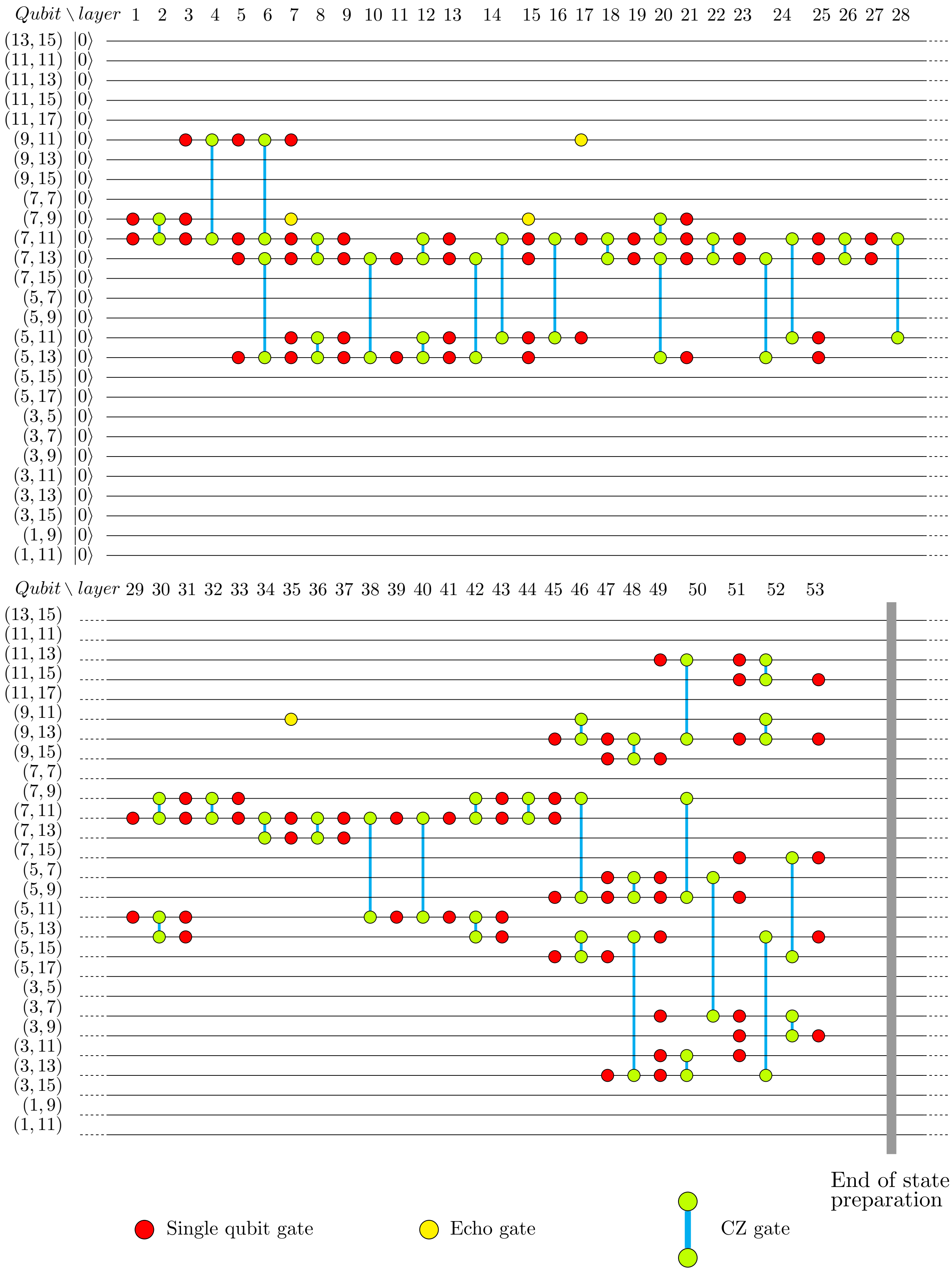

FIG. S15. Experimental circuit for preparing the ground state of the Fibonacci string-net model, which is obtained by variationally optimizing the original circuit shown in the main text Fig. 2**a** targeting the ideal state. The whole circuit contains 53 layers, with each layer containing only single- or two-qubit gates that are applied simultaneously. Each qubit is labeled by (row index, column index) as shown in the Extended Data Fig. 1 of the main text.

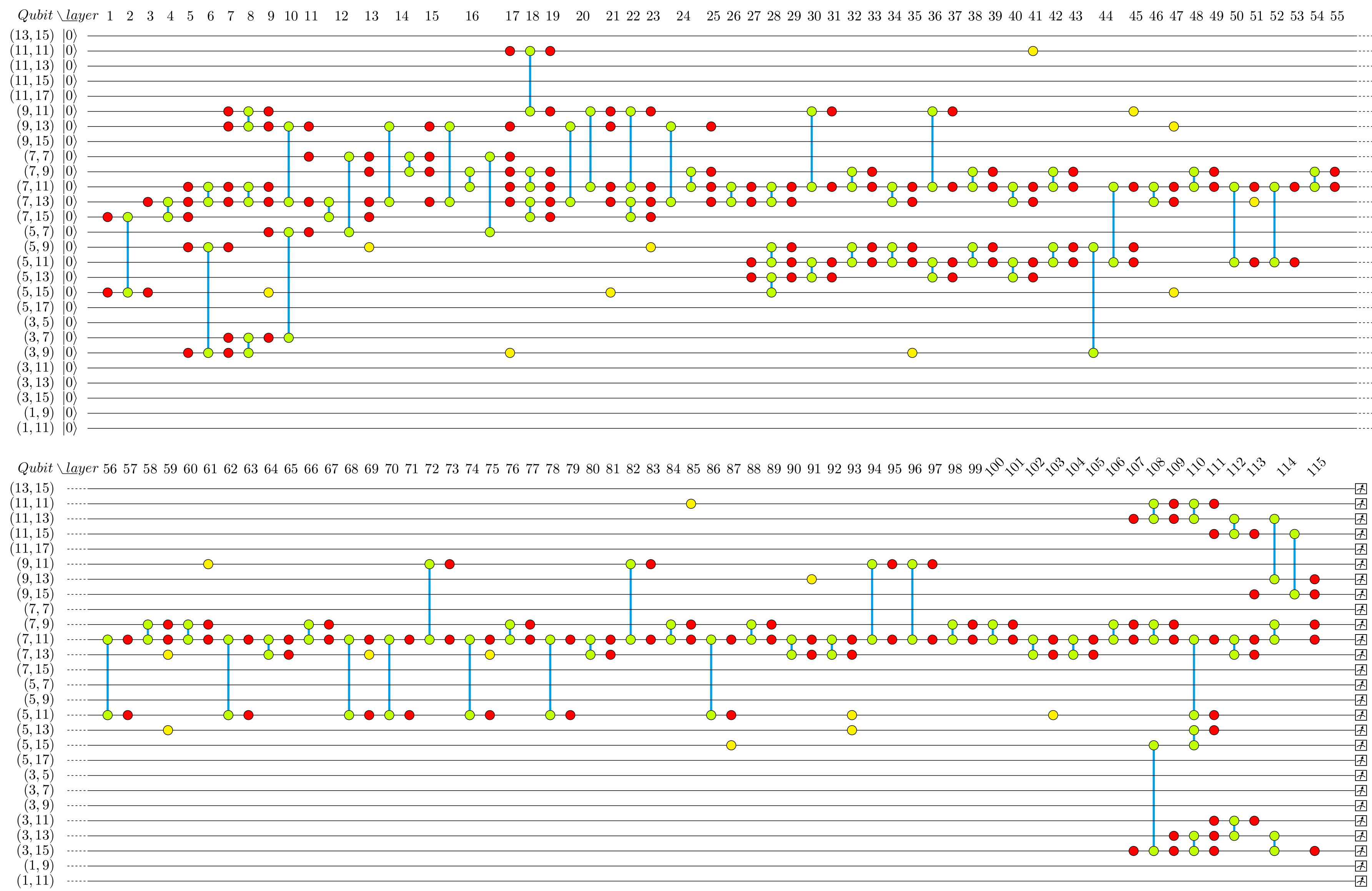

FIG. S16. Experimental circuit for preparing the ground state of the Fibonacci string-net model, which is obtained by variationally optimizing the F-move operations shown in the main text Extended Data Fig. 2. The whole circuit contains 115 layers, with each layer containing only single- or two-qubit gates that are applied simultaneously.

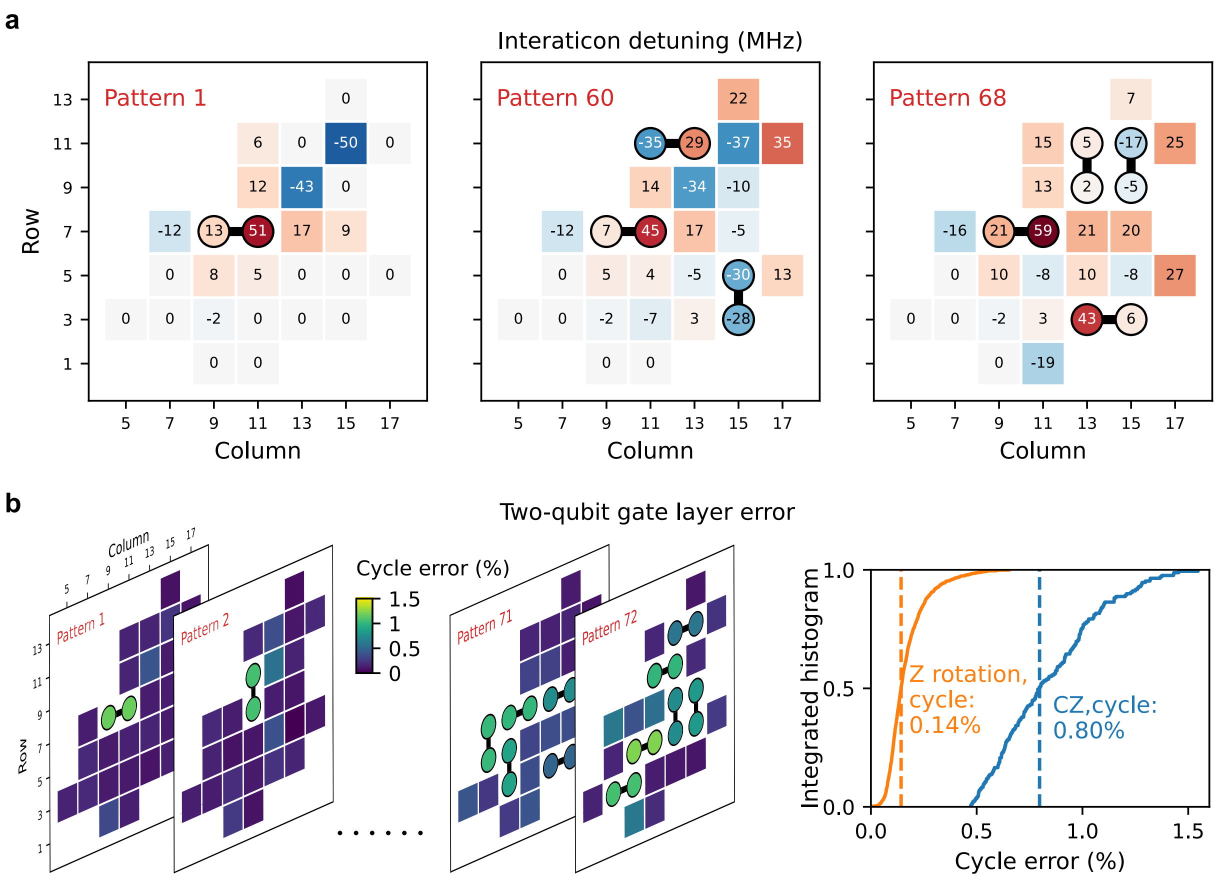

FIG. S17. Parameters of the two-qubit CZ gate layers. a, Optimal interaction frequencies for three typical two-qubit gate layers with different patterns of parallel CZ gates applied on the highlighted qubit pairs (circles connected with solid lines). Displayed are the detunings of the qubits from their idle frequencies. We note that the parameters of a CZ gate may be different in different patterns. **b**, Cycle errors of the CZ gates (with each cycle consisting of a CZ gate and two single-qubit gates) and Z rotations (with each cycle consisting of two single-qubit gates). We characterize the single- and two-qubit gate errors with simultaneous XEB for all the 72 two-qubit gate layers used in the experiment, with each layer corresponding to a unique pattern of parallel CZ gates. The corresponding integrated histogram of the cycle errors for all the CZ gates and Z rotations are shown in the right. Dashed lines indicate the median values.

of the rest qubits are characterized with the method shown in Fig. S18 and canceled out with virtual Z gates. The Pauli errors of all the CZ gates in the experimental circuit, characterized by the simultaneous XEB, are shown in Fig. S17b, c, with a median value of 6.6e-3.

C. Topological entanglement entropy measurement

For the string-net states studied in this experiment, the topological entanglement entropy can be calculated either from the von Neumann entropy

$$S_i = -\mathrm{Tr}(\rho_i \ln \rho_i), \tag{S41}$$

or the Rényi entropy of arbitrary order α (up to a negligible term of order $O(\exp(-L))$ with L being the boundary length)

$$S_{\alpha,i} = \frac{1}{1-\alpha} \ln \mathrm{Tr}(\rho_i^{\alpha}), \tag{S42}$$

where ρ_i is the density matrix of the subsystem $i \in \{A, B, C, AB, AC, BC, ABC\}$ [23]. The difference of the entanglement entropy calculated by the two choices for the system considered in this experiment is shown in Fig. S19. The experimental

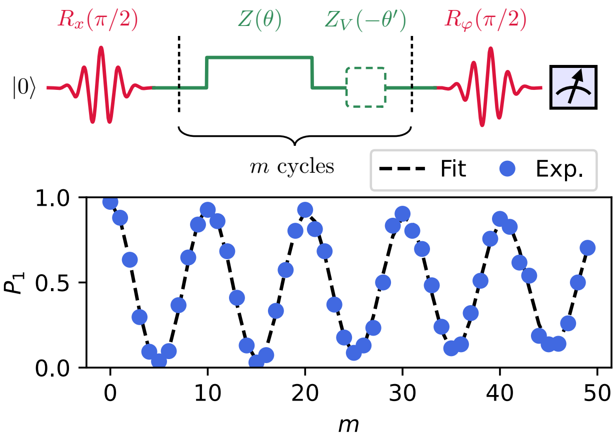

FIG. S18. Calibration of the compensated virtual Z gate in the two-qubit gate layer. Top panel: The pulse sequence to amplify the tiny angle $\theta - \theta'$. We model the applied z pulse on the idle qubit during the execution of the two-qubit gate layer as a Z rotation $Z(\theta)$ which can be compensated with a virtual Z rotation $Z_V(-\theta')$ when $\theta - \theta' = 0$. The final xy rotation $R_\varphi(\pi/2)$ is designed to detect the amplified angle $m(\theta - \theta')$ where the subscript φ refers to an equatorial rotation axis that has an angle φ with respect to the x-axis. In practice, φ is chosen as $0.2m\pi$ where m is the cycle number and the corresponding oscillation frequency of the measured probability of $|1\rangle$ is predicted as $f = 0.1 + (\theta - \theta')/(2\pi)$. Bottom panel: Example experimental data. We fit the data with the damped oscillation: $A \cdot \cos(2\pi f \cdot m + \Theta) \cdot e^{-\Gamma m} + B$. Note that the calibration can be performed simultaneously on multiple qubits.

characterization of a density matrix is resource-consuming, with cost typically growing exponentially with the qubit number. Alternatively, we can measure the second-order Rényi entropy using the randomized measurement (RM) protocols [24] without reconstructing the whole density matrix and thus reducing the required sampling number. Moreover, the RM method can extract all the entropies for different subsystems from the same data, which further reduces the required experimental resources. The core of RM is to obtain a set of classical representations of the target state by applying random unitary operations before measuring all the qubits on the computational basis. The second-order Rényi entropy can be predicted from the obtained classical data with high accuracy.

The RM method requires analyzing the statistical correlations between the outcomes of measurements performed after random unitaries, and the estimator for the second-order Rényi entropy takes the following form:

$$\mathrm{Tr}(\rho_i^2) = 2^{N_i} \sum_{w,w'} (-2)^{-H(w,w')} \overline{P(w)P(w')}, \tag{S43}$$

where N_i and ρ_i are the qubit number and density matrix of the subsystem i. w, w' are the binary strings and $H(w, w')$ is the hamming distance between them. $P(w)$ denotes the probability of observing w. The average is over different random unitaries in RM.

In practice, there are two choices of random unitaries in RM, which can be tensors of either single-qubit Haar-random rotations or single-qubit random Clifford rotations, with the latter being equivalent to random Pauli basis measurement. The performance of RM depends on the quantum state under study as well as the selection of random single-qubit gates. For the ground state of string-net model in this work, we numerically study the efficiency of the two choices. As shown in Fig. S19c, the RM results with Haar-random rotations exhibit both less deviation from the ideal value and less statistical fluctuation than those with random Clifford rotations. In our experiment, we apply RM with 1500 instances of Haar-random unitaries to obtain the second-order Rényi entropy.

The experimentally measured entanglement entropies are shown in Fig. 3 of the main text. Here, we further display all the values of the Rényi entropies and entanglement entropies with error bars estimated by bootstrapping (Fig. S20). For all the nine different subsystem configurations, the corresponding entanglement entropies are well below that of the Z_2 topological ordered state. In Fig. S21, we plot the scaling of the standard deviation of the topological entropy as a function of the instance size for different repetition number of projective measurements, which show good agreement with the experimental data.

We further verify the experimental results by performing quantum state tomography (QST) for the subsystem with qubit numbers less than 7, from which we obtain the density matrices and calculate the corresponding second-order Rényi entropies. In Fig. S22a, we plot the QST results on top of the RM results as displayed in the main text, which shows good agreement. The fidelities of the states are also shown in Fig. S22b.

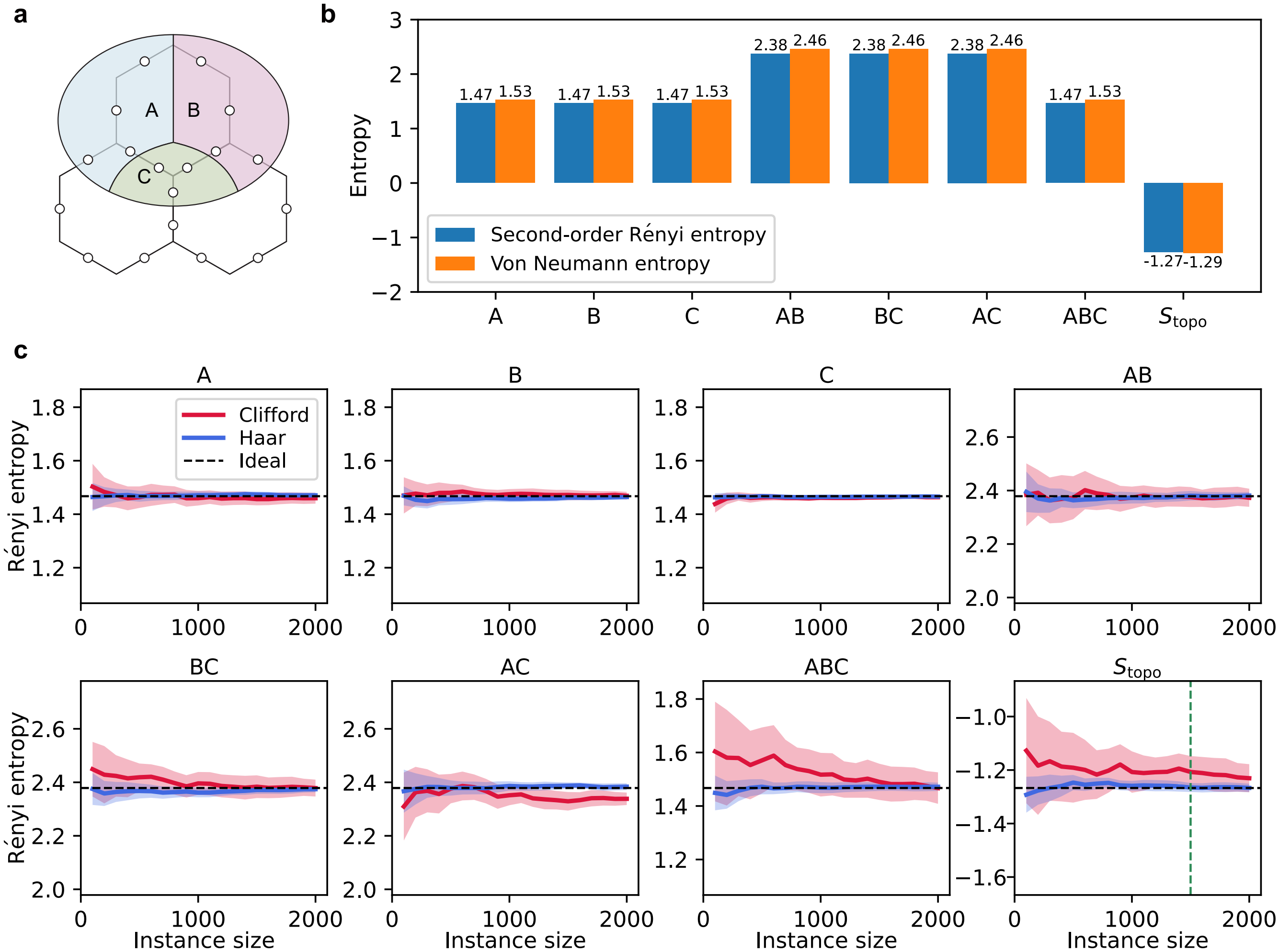

FIG. S19. Noiseless numerical simulation of the topological entanglement entropy. **a**, The three simply connected subregions A, B, and C that are used to extract the topological entropy. **b**, The comparison of the second-order Rényi entropies (blue) and Von Neumann entropies (orange) of all the subsystems and the corresponding topological entanglement entropy. The entropies of all the subsystems are calculated according to Eq. S42 and Eq. S41 with the numerically simulated density matrices. **c**, The comparison of RM protocols using Haar-random rotations and random Clifford rotations. For each random unitary instance size, we repeat Monte Carlo simulation for 20 times to obtain the average value (solid line) and the standard deviation (light color region). The black horizontal dash line represents the ideal value of the second-order Rényi entropy calculated with Eq. S42. The RM protocol using Haar-random rotations shows both less deviation from the ideal value and less statistical fluctuation. We use 1500 instances of Haar-random unitaries to obtain the second-order Rényi entropy in the experiment as indicated by the green vertical dash line in the right-down panel.

D. Readout error mitigation

In this experiment, we use the iterative Bayesian unfolding (IBU) method [25, 26] to mitigate the readout error. We first construct the response matrix $\mathcal{R}_{ij} = P(m = i|t = j)$ from the measured single-qubit readout fidelities [27], where $P(m = i|t = j)$ denotes the conditional probability of measuring the bitstring i when the truth is the bitstring j in the computational basis. Then we can extract the corrected probability by iteratively applying the following equation

$$c_i^{n+1} = \sum_j \frac{\mathcal{R}_{ji} c_i^n}{\sum_k \mathcal{R}_{jk} c_k^n} m_j, \tag{S44}$$

where m_i and c_i are the measured and corrected probabilities of bitstring i, respectively. In practice, c_i^0 are initialized as a uniform distribution and the iteration number is 50.

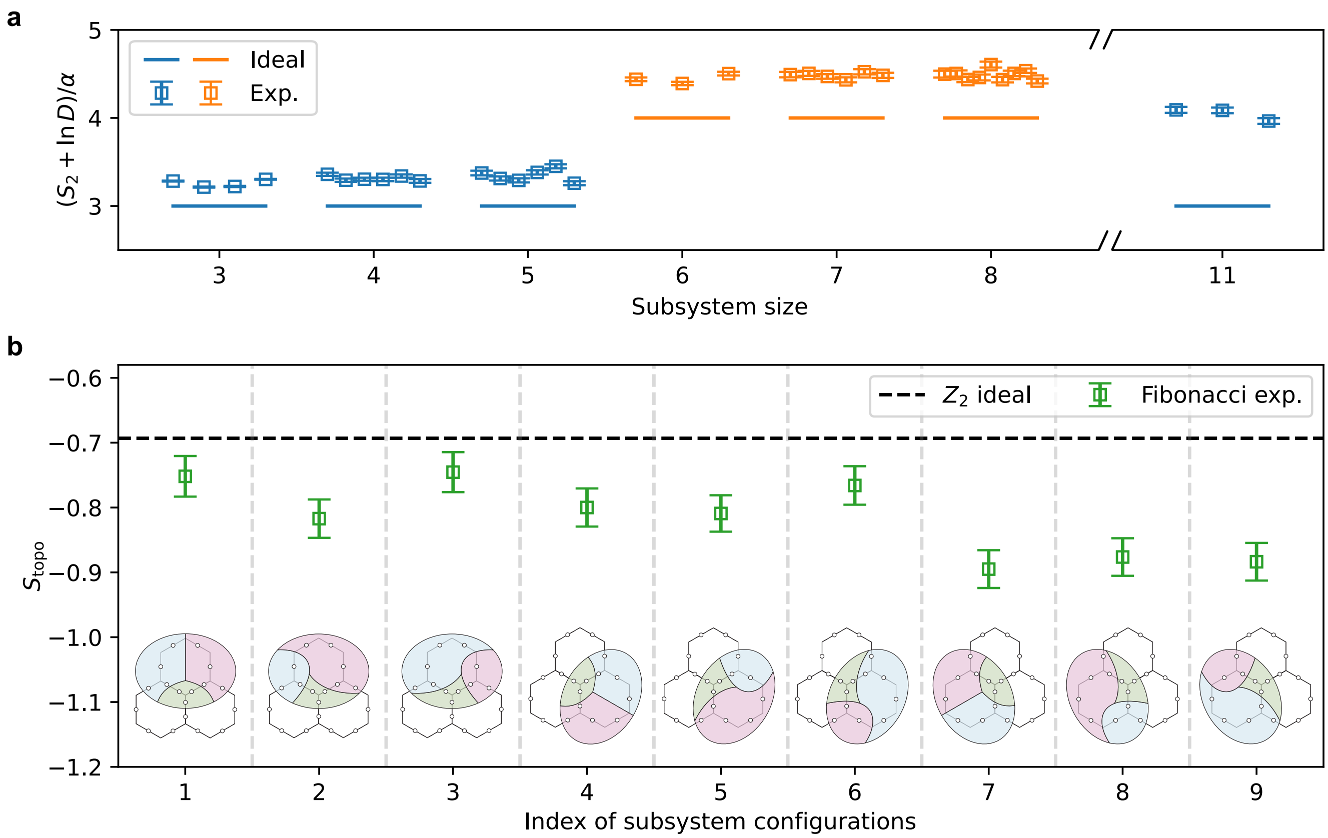

FIG. S20. Experimentally measured S_{topo} with error bars. **a**, Distribution of the rescaled second-order Rényi entropies with error bars representing the standard deviation. Here we use bootstrapping (resampling to form a 1500-instance dataset with replacement from 1500 instances of Haar-random unitaries for 100 times) to estimate the standard deviation. **b**, The individual values of nine different estimates of S_{topo} with error bars representing the standard deviation, with the corresponding subsystem configurations shown in the inset. The values of all nine S_{topo} are clearly smaller than the theoretical S_{topo} of the toric code Z_2 topologically ordered state.

Now we consider the error propagation in the IBU method. For a sampling experiment with n repetitions, the random variable $X^i = (\sum_{k=1}^{n} x_k^i)/n$ is an unbiased estimator for the measured probability m_i where

$$x_k^i = \begin{cases} 1, & \text{if sampled bitstring } i \\ 0, & \text{otherwise} \end{cases}. \tag{S45}$$

But the intuitive estimator $X^i X^j$ for $m_i m_j$ is actually biased since $E(X^i X^j) - Cov(X^i, X^j) = E(X^i)E(X^j) = m_i m_j$. For convenience, we represent the map from the vector of measured probabilities $\vec{m}$ to c_i as $c_i = f_i(\vec{m})$. Based on Taylor expansion, $f_i(\vec{X})$ can be approximated as $f_i(\vec{m}) + \sum_k J_{ik}(X^k - m_k)$ where $\vec{X}$ is the vector of X^i and $J_{ik} = \frac{\partial f_i}{\partial x_k}|_{\vec{x}=\vec{m}}$ is the element of the Jacobian matrix. Then we can calculate the following expectation

$$\begin{aligned} E[f_i(\vec{X})f_j(\vec{X})] \approx & f_i(\vec{m})f_j(\vec{m}) + f_i(\vec{m})\sum_k J_{ik}E(X^k - m_k) + f_j(\vec{m})\sum_l J_{jl}E(X^l - m_l) \\ & + \sum_{kl} J_{ik}E[(X^k - m_k)(X^l - m_l)]J_{jl} \\ = & c_i c_j + \sum_{kl} J_{ik} Cov(X^k, X^l) J_{lj}^T. \end{aligned} \tag{S46}$$

Note that the covariance $Cov(X^k, X^l)$ can be estimated with the following unbiased estimator

$$C_{kl} = \frac{\sum_i (x_i^k - X^k)(x_i^l - X^l)}{N(N-1)} = \begin{cases} [X^k - (X^k)^2]/(N-1), & k = l \\ -X^k X^l/(N-1), & k \neq l \end{cases}, \tag{S47}$$

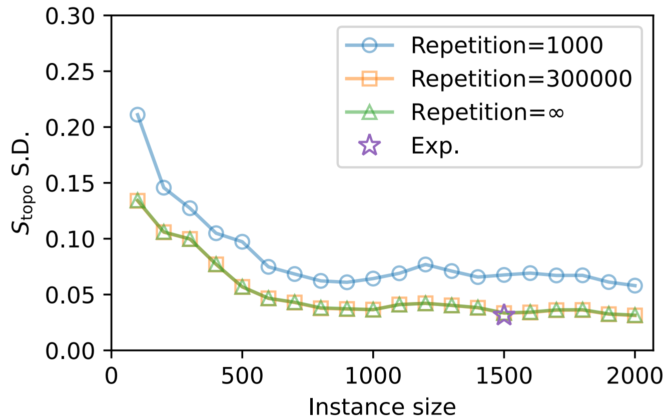

FIG. S21. Scaling of statistical errors with random unitary instance size. We plot the standard deviation (S.D.) of the entanglement entropy $S_{\rm topo}$ of the first subsystem configuration as a function of the instance size for various repetition number of projective measurements. The standard deviations are calculated by repeating the numerical simulation for 20 times. Here, repetition=∞ represents the ideal values. From this figure, the statistical error induced by the limited repetition number of projective measurements becomes negligible when repetition=300000.

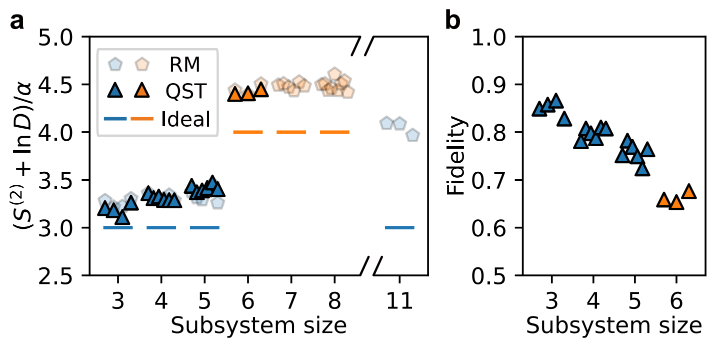

FIG. S22. Experimental comparison of the second-order Rényi entropies extracted from RM and quantum state tomography (QST). a, Distribution of the rescaled second-order Rényi entropies. We characterize the density matrices for all subsystems with qubit numbers less than seven using QST and then calculate the second-order Rényi entropies according to Eq. S42. The extracted data are displayed on top of the RM results as displayed in the main text Fig. 3**b**. As expected, the QST results are in good agreement with the RM results. **b**, The fidelities (defined as $(\mathrm{Tr}\sqrt{\sqrt{\rho_{\rm ideal}}\rho_{\rm exp}\sqrt{\rho_{\rm ideal}}})^2$) of the experimentally obtained density matrices $\rho_{\rm exp}$ compared with the corresponding ideal ones $\rho_{\rm ideal}$.

and the Jacobian matrix can be obtained with JAX [28]. From Eq. S46 and Eq. S47 we can estimate $P(i)P(j)$ appeared in Eq. S43 with $f_i(\vec{X})f_j(\vec{X}) - \sum_{kl} J_{ik}C_{kl}J^T_{lj}$ which converges faster than $f_i(\vec{X})f_j(\vec{X})$ and fewer repetitions are needed (see Fig. S23).

[1] F. Wilczek, Quantum mechanics of fractional-spin particles, Phys. Rev. Lett. **49**, 957 (1982).
[2] C. Nayak, S. H. Simon, A. Stern, M. Freedman, and S. Das Sarma, Non-abelian anyons and topological quantum computation, Rev. Mod. Phys. **80**, 1083 (2008).
[3] J. Preskill, Lecture notes for physics 219: Quantum computation, available at http://www.theory.caltech.edu/preskill/ph219/ph219_2004.html (2004).
[4] A. Y. Kitaev, Fault-tolerant quantum computation by anyons, Ann. Phys. **303**, 2 (2003).
[5] M. A. Levin and X.-G. Wen, String-net condensation: A physical mechanism for topological phases, Phys. Rev. B **71**, 045110 (2005).
[6] C.-H. Lin, M. Levin, and F. J. Burnell, Generalized string-net models: A thorough exposition, Phys. Rev. B **103**, 195155 (2021).
[7] A. Schotte, G. Zhu, L. Burgelman, and F. Verstraete, Quantum error correction thresholds for the universal fibonacci turaev-viro code, Phys. Rev. X **12**, 021012 (2022).
[8] Z. Wang, X.-L. Qi, and S.-C. Zhang, Topological order parameters for interacting topological insulators, Phys. Rev. Lett. **105**, 256803

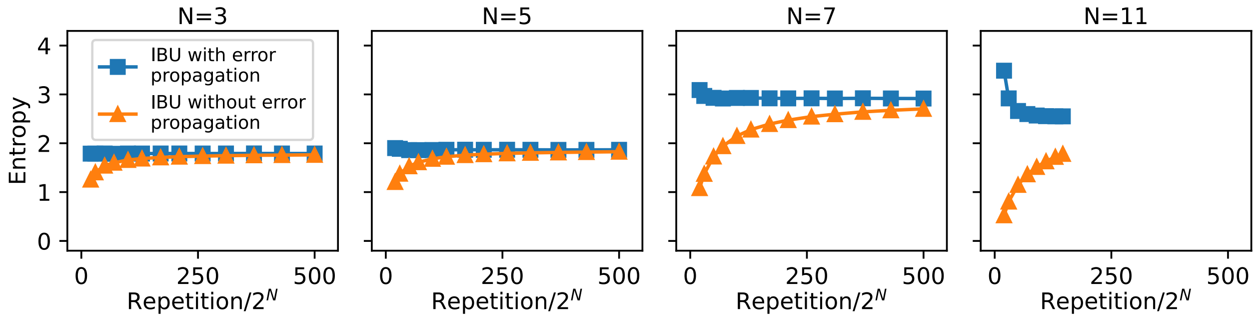

FIG. S23. The second order Rényi entropy of different subsystem size N. We compare the mitigated entropy using the IBU method with (blue square) and without (orange triangle) error propagation. Faster convergence is observed with error propagation and fewer repetitions are needed which are extremely resource-consuming. All data are extracted from the same experimental dataset with 300000 repetitions and 1500 instances.

(2010).

[9] R. König, B. W. Reichardt, and G. Vidal, Exact entanglement renormalization for string-net models, Physical Review B **79**, 195123 (2009).

[10] N. E. Bonesteel and D. P. DiVincenzo, Quantum circuits for measuring Levin-Wen operators, Phys. Rev. B **86**, 165113 (2012).

[11] Y. Hu, N. Geer, and Y.-S. Wu, Full dyon excitation spectrum in extended Levin-Wen models, Phys. Rev. B **97**, 195154 (2018).

[12] A. Kitaev, Anyons in an exactly solved model and beyond, Ann. Phys. **321**, 2 (2006).

[13] M. Levin and X.-G. Wen, Detecting topological order in a ground state wave function, Phys. Rev. Lett. **96**, 110405 (2006).

[14] A. Kitaev and J. Preskill, Topological entanglement entropy, Phys. Rev. Lett. **96**, 110404 (2006).

[15] K. Satzinger, Y.-J. Liu, A. Smith, *et al.*, Realizing topologically ordered states on a quantum processor, Science **374**, 1237 (2021).

[16] N. A. Nemkov, E. O. Kiktenko, I. A. Luchnikov, and A. K. Fedorov, Efficient variational synthesis of quantum circuits with coherent multi-start optimization, Quantum **7**, 993 (2023).

[17] S. Xu, Z.-Z. Sun, K. Wang, *et al.*, Digital simulation of projective non-abelian anyons with 68 superconducting qubits, Chin. Phys. Lett. **40**, 060301 (2023).

[18] C. Song, K. Xu, W. Liu, C.-p. Yang, S.-B. Zheng, H. Deng, Q. Xie, K. Huang, Q. Guo, L. Zhang, *et al.*, 10-qubit entanglement and parallel logic operations with a superconducting circuit, Phys. Rev. Lett. **119**, 180511 (2017).

[19] D. C. McKay, C. J. Wood, S. Sheldon, J. M. Chow, and J. M. Gambetta, Efficient z gates for quantum computing, Phys. Rev. A **96**, 022330 (2017).

[20] W. Ren, W. Li, S. Xu, *et al.*, Experimental quantum adversarial learning with programmable superconducting qubits, Nat. Comput. Sci. **2**, 711 (2022).

[21] M. Treinish, Qiskit/qiskit: Qiskit 0.39.2 (2022).

[22] P. V. Klimov, J. Kelly, J. M. Martinis, and H. Neven, The snake optimizer for learning quantum processor control parameters (2020), arXiv:2006.04594 [quant-ph].

[23] S. T. Flammia, A. Hamma, T. L. Hughes, and X.-G. Wen, Topological entanglement Rényi entropy and reduced density matrix structure, Phys. Rev. Lett. **103**, 261601 (2009).

[24] T. Brydges, A. Elben, P. Jurcevic, *et al.*, Probing Rényi entanglement entropy via randomized measurements, Science **364**, 260 (2019).

[25] G. D'Agostini, A multidimensional unfolding method based on bayes' theorem, Nuclear Instruments and Methods in Physics Research Section A: Accelerators, Spectrometers, Detectors and Associated Equipment **362**, 487 (1995).

[26] B. Nachman, M. Urbanek, W. A. de Jong, and C. W. Bauer, Unfolding quantum computer readout noise, npj Quantum Inf. **6**, 84 (2020).

[27] Y. Zheng, C. Song, M.-C. Chen, *et al.*, Solving systems of linear equations with a superconducting quantum processor, Phys. Rev. Lett. **118**, 210504 (2017).

[28] J. Bradbury *et al.*, JAX: composable transformations of Python+NumPy programs (2018).